



Full length article

Thermal conductivity of architected cellular metamaterials

A. Mirabolghasemi ^a, A.H. Akbarzadeh ^{a,b,*}, D. Rodrigue ^c, D. Therriault ^d^a Department of Bioresource Engineering, McGill University, Island of Montreal, QC, H9X 3V9, Canada^b Department of Mechanical Engineering, McGill University, Montreal, QC, H3A 0C3, Canada^c Department of Chemical Engineering, Université Laval, Quebec, QC, G1V 0A6, Canada^d Department of Mechanical Engineering, Polytechnique Montreal, Montreal, QC, H3C 3A7, Canada

ARTICLE INFO

Article history:

Received 10 October 2018

Received in revised form

28 February 2019

Accepted 30 April 2019

Available online 7 May 2019

Keywords:

Architected cellular metamaterials

Effective thermal conductivity

Homogenization

Supershape pore

Thin-walled open lattice

Shellular materials

Functionally graded cellular materials

ABSTRACT

Periodic architected cellular metamaterials, as a novel class of low-density materials, possess unprecedented multifunctional properties mainly due to their underlying microarchitecture. In this paper, we study the thermal conductivity of cellular metamaterials and evaluate their performance for thermal management applications. To understand the relations between the microarchitecture and the thermal response, we analyze the thermal conductivity of a wide range of cellular metamaterials with strategically developed microarchitectures from two-dimensional (2D) cells with Supershape pores to three-dimensional (3D) thin-walled open lattices and shellular materials. We implement standard mechanics homogenization on the periodic representative volume elements (RVEs) of these cellular metamaterials to examine the effect of pore architecture (relative density, pore shape, pore orientation, and pore elongation) on their effective thermal conductivity. The numerical results show how the thermal conductivity of an isotropic material can be modified by pore introduction and how the pore architecture could lead to an anisotropic effective thermal conductivity tensor. To examine the impact of having 2D Supershape cuts on 3D RVEs, thin-walled open lattices are designed as an assembly of thickened 2D RVEs with Supershape pores. A mathematical model is derived based on the effective thermal properties of the constituent 2D RVEs to predict the effective thermal properties of these lightweight cellular materials. Effective thermal conductivity of shellular materials based on triply periodic minimal surfaces is also compared with those of the previously introduced architectures. Unlike the shellular materials, which only cover a narrow region of thermal conductivity versus relative density chart, cellular materials with a wide range of anisotropic effective thermal conductivities can be engineered by using 2D Supershape pores on 2D or 3D thin-walled cells. Finally, we show how the concept of architected functionally graded cellular materials can be used to tune the heat flow within cellular media to guide it in a specific direction to control the temperature inside advanced 3D printed materials. As a case study, the optimum spatial distribution of pore rotation angle is found to maximize or minimize the heat flow passing through different sides of a square-shaped porous slab. This paper opens an avenue for developing thermal metamaterials with programmable anisotropic thermal properties.

© 2019 Acta Materialia Inc. Published by Elsevier Ltd. All rights reserved.

1. Introduction

Developing lightweight and structurally robust advanced materials with unprecedented multifunctional properties has been one of the main engineering challenges during the past few

decades. Limited material and energy resources, economical restrictions, and concerns over the prospect of climate changes promote the design and manufacturing of durable lightweight materials with tunable multifunctional properties. The engineered materials with properties not available in natural materials are called *metamaterials*, among which bio-inspired architected cellular materials [1] are one of the cutting-edge lightweight and optimized materials that can simultaneously satisfy multiple functionalities from structural stiffness to thermal insulation or heat exchanging [2].

Cellular materials are divided into two categories: (1) Foams

* Corresponding author. Department of Bioresource Engineering, McGill University, Island of Montreal, QC, H9X 3V9, Canada.

E-mail address: hamid.akbarzadeh@mcgill.ca (A.H. Akbarzadeh).

URL: <https://www.mcgill.ca/bioeng/faculty-and-staff/abdolhamid-akbarzadeh-shafaroudi>

where a gaseous phase is randomly dispersed in a continuous solid medium, and (2) Periodic porous materials (lattices) which consist of a periodic architected cell [3]. Inspired by their excellent light-weight and mechanical properties, natural materials like bone, wood, and cork led to the development of cellular materials as early as 1970. Hexagonal honeycombs as sandwich cores, used in aviation industry, is one of the first applications of periodic cellular materials [4]. Driven by the high performance of cellular materials and recent developments in advanced manufacturing techniques, such as additive manufacturing (3D printing) and laser cutting, advanced polymeric and metallic cellular materials with complex nano/microarchitectures can be designed and fabricated. A non-exhaustive list of applications of cellular materials found in the literature includes: lightweight structural elements in aircrafts and high-speed trains, energy-absorbing elements in automotive industry, thermal insulators, thermal energy storage devices, hydrogen storage tanks, and biomedical scaffolds for tissue engineering [3–12].

To exploit the multifunctional potentials of cellular materials, a mathematical model capable of accurately predicting their effective properties is of crucial importance. Early efforts on this subject range from the simple volumetric averaging of properties of constituent materials, the so-called *rule of mixtures method*, to several empirical equations to predict the physical properties of cellular materials [3,13]. Investigations have clearly shown that cell microarchitecture, in addition to the constituent materials properties, plays a significant role in the emergence of the exotic properties of cellular materials, such as negative Poisson's ratio in auxetic materials [14] and thermal and vibration insulation properties of ultralight metallic microlattices [15]. In this regard, since thermal conductivity, electrical conductivity and magnetic permeability are all mathematically described by Laplace equation, existing approaches used in the electric and magnetic fields have also been applied to predict the thermal properties of cellular materials [16,17]. The introduction of the thermal-circuit method, based on the analogy between electrical and thermal conductivities, can be considered as a turning point in the theoretical modelling of thermal conductivity of cellular materials [17]. It is worth mentioning that most of the analytical models have been mainly developed for porous materials with random pore distribution [18], or for periodic cellular materials with simple pore topologies: i.e. cubic, circular, cylindrical and spherical pore shapes [5,19], leaving cellular materials with complex periodic microarchitectures and potentially superior multifunctional properties unexplored. Although analytical upper and lower bounds, e.g. Hashin-Shtrikman bounds [20] or bounds obtained by the thermal-circuit method, are valuable for estimating the effective thermal conductivity with a minimum knowledge about the actual heat flow and temperature profile within cellular materials, advanced computational models, e.g. lattice-based Monte Carlo approach [21], micropolar modelling [22], as well as standard mechanics [23] and asymptotic [24] homogenization techniques have been introduced to precisely take into account the effect of micro-architecture of cellular materials in order to accurately predict their effective thermal properties.

Although the main focus of the literature on cellular materials has been devoted to their mechanical properties, the connection between cell microarchitecture and their effective thermal conductivity has also been the subject of compelling research over the past few decades. The analysis of the anisotropic thermal behavior of cellular metals [7], studies on thermal properties of new architected materials such as shellular materials [25,26], invention of thermal metamaterials to manipulate heat at a continuum level [27], and research on thermal properties of nanostructured cellular materials [28–30], are a few examples of the research in thermal

analysis of architected cellular solids. However, to the best of the authors' knowledge, apart from cells with simple pore shapes, no in-depth study on the relation between topological parameters and the thermal conductivity tensor of periodic cellular metamaterials with complex pore microarchitectures has been performed. As a result, a deeper understanding of the thermal properties of cellular materials is required to address the thermal requirements of emerging technologies such as lightweight electronics and catalysts.

In this paper, after introducing various cell architectures in Section 2, two methodologies for predicting the effective thermal conductivity of 2D cellular materials are discussed in section 3: (1) Theoretical modelling using the thermal-circuit method [31] and (2) Computational modelling based on standard mechanics homogenization. In Section 4, after investigating the validity of assumptions made in previous sections, we first compare the aforementioned two methodologies to predict the effective thermal conductivity of 2D cellular metamaterials with rectangular and elliptic pores. While the theoretical model can at best provide narrow bounds for the effective thermal conductivity of architected cellular metamaterials with simple 2D microarchitectures, standard mechanics homogenization is used to accurately determine the thermal conductivity of cellular metamaterials with complex 2D pore topologies of Supershape pores [32] (introduced in section 2.1). In addition to an in-depth analysis on the effects of topological parameters (pore shape, pore scaling, and pore rotation) on the effective thermal conductivity of these 2D architected cellular materials, a case study is conducted to highlight the importance of the off-diagonal terms of the anisotropic thermal conductivity tensor for the thermal analysis of cellular metamaterials. Thereafter, a mathematical model based on superposition is derived to predict the thermal conductivity of lightweight 3D thin-walled open lattices (systematically designed in section 2.2) based on the effective thermal conductivity of 2D Supershape architectures. Following the recent interests in periodic minimal surfaces in material engineering, the thermal conductivities of thin-walled metamaterials are compared with three shellular materials which are lightweight microarchitectures based on triply periodic minimal surfaces (presented in Section 2.3). While the shellular materials in this work exhibit isotropic effective thermal conductivities, the anisotropic thermal properties of thin-walled open lattices show possibilities for better use of cellular materials to optimize the thermo-mechanical performance of lightweight structures. Finally, in a case study conducted in Section 5, pore angle inside a 2D cellular medium is graded to optimize the heat flow passing through its different edges, showing how grading the cells throughout porous media provides new alternatives for optimizing thermal performance of advanced materials.

2. CAD design of architected cellular metamaterials

To apply a computational homogenization method and explore the effects of pore topology and relative density on the effective thermal conductivity of cellular metamaterials, two-dimensional (2D) square representative volume elements (RVEs) with Supershape pores, 3D cubic thin-walled open lattices cut through by 2D Supershape pores on opposite faces, and shellular RVEs are examined.

2.1. 2D supershape RVEs

As a powerful formula for creating a wide variety of pore topologies, the *Superformula* [32], is selected and modified to generate alternative pore architectures, while scaling (S) and rotation (β) are considered to increase the possibilities of pore

topologies. The boundary of this Supershape pore in a Cartesian coordinate system is mathematically expressed as:

$$\begin{bmatrix} x_0 \\ y_0 \end{bmatrix} = \begin{bmatrix} \cos \beta & -\sin \beta \\ \sin \beta & \cos \beta \end{bmatrix} \left([|\cos(m\alpha/4)| + |\sin(m\alpha/4)|]^n \begin{bmatrix} S \cos(\alpha) \\ \sin(\alpha) \end{bmatrix} \right) \quad (1)$$

($-\pi \leq \alpha \leq \pi$, $m = 1 \sim 8$, $n = -5 \sim 5$, $S = 1 \sim 3.5$ (0.5 increment), $0 \leq \beta \leq \pi/2$)

As introduced in Eq. (1), a pore gets elongated along the x direction by increasing the scaling factor S , followed by a counter-clockwise rotation of β degree. Using Eq. (1), the area of the pore can be calculated by $4S \int_0^{\frac{\pi}{4}} (\cos \gamma + \sin \gamma)^{2n} d\gamma$ independent of the values of β and m . When no scaling exists ($S = 1$), m defines the pore order of rotational symmetry, meaning that rotating the pore by an angle of $360^\circ/m$ does not change it.

To focus on 2D architected closed-cell metamaterials, one percent of the RVE's length is selected as the minimum allowable clearance between the pore and RVE's outer edges to avoid pore walls from touching the RVE's boundaries. For these 2D metamaterials, porosity (Φ) is defined as the ratio between the pore area and the whole cell area, which in the case of a unit square RVE, is equal to the pore area. On the other hand, relative density (ρ_r) is defined as the ratio of the solid area to the whole cell area and is equal to: $1 - \Phi$. For a unit square RVE with an enclosed 2D Supershape pore, Eq. (1) can be rewritten in terms of the relative density (ρ_r) via $\begin{bmatrix} x \\ y \end{bmatrix} = \begin{bmatrix} x_0 \\ y_0 \end{bmatrix} \sqrt{(1 - \rho_r)/(SA_0)}$, where A_0 for different n values is reported in Table 1.

Fig. 1 presents typical RVEs of the 2D architected cells for different topological parameters. Each pore topology, corresponding to each set of geometrical parameters introduced in Eq. (1), is modeled within ANSYS APDL (Fig. S.1 of Supplementary Document) by creating keypoints and using spline curves. The area surrounded by the splines is formed, scaled, rotated and moved to the center of the RVE to be subtracted from the unit solid RVE and to create 2D Supershape cellular metamaterials.

lightweight thin-walled open lattice architectures, based on 2D Supershape pore topologies, are introduced and their effective

thermal conductivity are compared with the thermal conductivity of 2D and 3D cellular materials. The 2D Supershape pores are cut from each face of a hollow cubic RVE with a total relative wall thickness equal to 2–10% of the RVE's length ($t_r = 0.02–0.1$). To fulfill geometrical periodicity, opposite faces of RVE are cut by identical pore shapes. As illustrated in Fig. 2b, with three different 2D pore shapes on the faces of cubic RVE, the number of achievable 3D thin-walled open cells is much higher than their 2D closed-cell counterparts. Considering the fact that 3D computer-aided design (CAD) and finite element modellings are more computationally expensive than 2D RVEs, a tighter limit for the geometrical parameters of Supershape pores is adopted ($1 \leq m \leq 4$, $-3 \leq n \leq 3$ and $S = 1$) and the pore's topological parameters are kept constant on all faces of the 3D thin-walled open lattices (Fig. 2c).

2.3. 3D shellular RVEs

A *Triply Periodic Minimal Surface* (TPMS) is a non-self-intersecting surface in R^3 , which has a crystalline structure repeated in three independent directions, having a zero mean curvature at each point [33]. The presence of TPMS in natural materials, like biological membranes [34] and crystals [33], has inspired researchers to consider TPMS architectures in tissue engineering and biomimetic material design [35–38]. The *shellular* term has been recently used in the literature to represent thin TPMS cellular shells. Among many known TPMSs, Schwarz's Primitive (P), Diamond (D), and Schoen's Gyroid (G) are selected here for analysis. These surfaces can be trigonometrically approximated using the following level surface equations [39]:

$$\begin{aligned} P: & \cos x + \cos y + \cos z = f \quad (f = 0, 0.4, 0.8) \\ D: & \sin x \sin y \sin z + \sin x \cos y \cos z + \cos x \sin y \cos z + \cos x \cos y \sin z = f \quad (f = 0) \\ G: & \cos x \sin y + \cos y \sin z + \cos z \sin x = f \quad (f = 0) \end{aligned} \quad (2)$$

2.2. 3D thin-walled open lattices

Using closed 3D surface equations (such as 3D Supershape formula) to generate 3D void shapes enables a parametric control over the pore geometry to create a variety of 3D RVEs for cellular materials. However, this method is generally unable to produce cells with low relative densities. To address this limitation, novel

We developed a MATLAB code to solve the level surface equations and determine the coordinates of several points on the surface. These points together with multiple cross-section curves, satisfying the surface equations, are firstly created inside SolidWorks using a Visual Basic code and then used to create a smooth surface. This part of the surface is then patterned to create the mid-surface of the shellular RVE and the pattern is subsequently

Table 1

A_0 for different n values.

n	-5	-4	-3	-2	-1	0	1	2	3	4	5
A_0	0.527	0.686	0.933	1.333	2.000	3.142	5.142	8.712	15.187	27.078	49.140

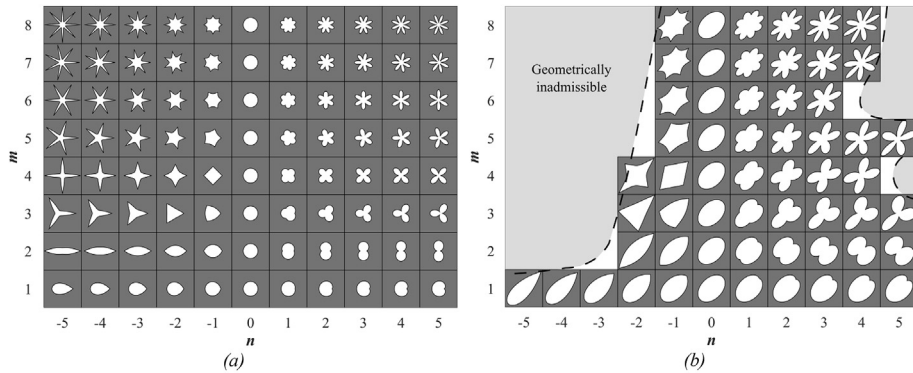


Fig. 1. Sample RVEs of 2D architected cellular metamaterials for different topological parameters: (a) $\rho_r = 0.88$, $S = 1$ and $\beta = 0^\circ$ and (b) $\rho_r = 0.62$, $S = 1.5$ and $\beta = 45^\circ$.

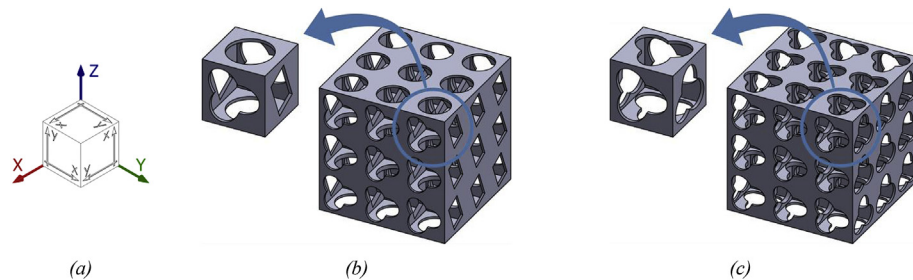


Fig. 2. (a) Local coordinate system used for the creation of 2D Supershape pores on each face of 3D RVE, (b) Possible thin-walled open lattice modeled in SolidWorks, and (c) Schematic view of a thin-walled open lattice considered in this study.

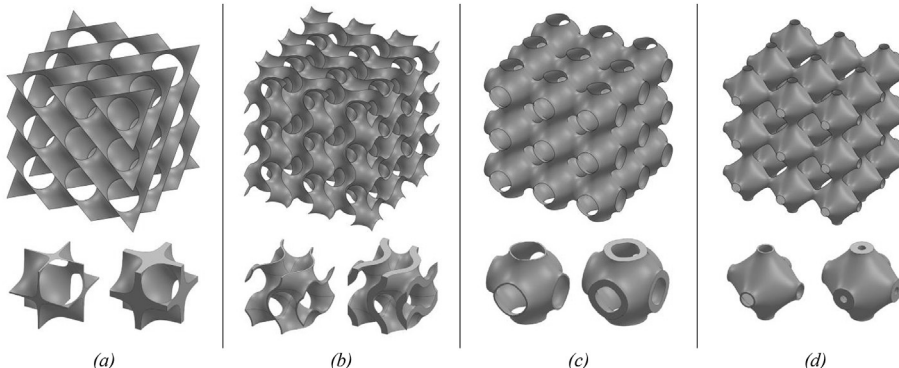


Fig. 3. $3 \times 3 \times 3$ TPMS cells together with two shellular RVEs at 0.02 and 0.10 relative thicknesses: (a) Schwarz D, (b) Gyroid, (c) Schwarz P with $f = 0$, and (d) Schwarz P with $f = 0.8$.

Table 2
Relative density of the shellular architectures, together with the relative surface area of their underlying minimal mid-surface.

	P ($f = 0$)	P ($f = 0.4$)	P ($f = 0.8$)	D ($f = 0$)	G ($f = 0$)	
$t_r = 0.02$	0.047	0.046	0.041	0.038	0.062	Relative density of the shellular architectures
$t_r = 0.06$	0.141	0.137	0.124	0.115	0.185	
$t_r = 0.1$	0.233	0.227	0.205	0.191	0.305	
($t_r = 0$)	2.35	2.29	2.08	1.92	3.09	Relative surface area of the TPMS

thickened to add the desired thickness (as shown in Fig. S.2 in Supplementary document). To focus on lightweight structures, five relative thicknesses (t_r) from 2 to 10% of RVE's length are considered for analysis. Some of the selected shellular architectures are presented in Fig. 3.

The relative surface area of the P, D and G TPMS can be defined by the ratio of the area of these surfaces inside their RVEs to the area of one face of the RVE. As the relative thicknesses of the shellular architectures are assumed to be less than 0.1 in this manuscript, by ignoring the curvature of their underlying TPMS mid-surfaces, their relative densities can be estimated by

multiplying the relative thickness and the relative surface area of the corresponding TPMS. The error associated with this method is found to be less than 1.5%. Relative densities of the shellular architecture, together with the relative surface areas of their underlying minimal surfaces are provided in Table 2.

3. Predictive methods

Fourier's law assumes the following linear relation between the heat flux (\vec{q}) and temperature gradient (∇T) through a symmetric

thermal conductivity tensor (K_{eff}):

$$\vec{q} = -K^{\text{eff}} \vec{\nabla} T \quad (3)$$

For 3D materials, thermal conductivity tensor can be written as a symmetric 3×3 matrix K , in which $K_{ij} = K_{ji}$. Each of the diagonal components (K_{ii}) relates temperature gradient along the corresponding primary direction of the coordinate system and heat flux in that direction. As a result, K_{ii} elements shall always be positive, regardless of the orientation of the coordinate system. Off-diagonal components (K_{ij}) of the thermal conductivity tensor represent the coupling effect between temperature gradient along one direction and heat flux normal to that direction. Therefore, depending on the orientation of the coordinate system, K_{ij} elements can be negative, zero, or positive. For thermally isotropic homogenous solid materials, K^{eff} tensor reduces to kI , where I is the identity tensor and k is the isotropic thermal conductivity. However, in the case of cellular materials, the overall thermal conductivity is generally anisotropic and depends on micro-architectural parameters of the cells [2].

Since the simple volumetric averaging approach is indifferent to cell architecture, it is unable to capture the anisotropic thermal properties of cellular materials and can misestimate the effective thermal conductivity. To address these shortcomings, several analytical and computational methods have been developed, among which the thermal-circuit method (or Resistor approach) has been widely used to predict the theoretical upper and lower bounds of thermal conductivity for a given cell topology [5,31]. More advanced numerical methods, e.g. computational homogenization, are required to exactly model the microarchitecture of cellular materials and accurately determine all components of the effective thermal conductivity tensor.

It should be noted that the contribution of heat transfer mechanisms other than conduction, i.e. radiation and convection, is assumed to be small and consequently neglected in this paper. For a cellular material made by a highly-conductive matrix and empty voids or gaseous inclusions, this assumption is valid for small pore sizes working close to the ambient temperature [5,40–43]. For highly porous cellular insulators made of less conductive base materials (such as polyurethane foams with porosities greater than 0.8), it has been reported that the radiation may contribute to up to 26% of the overall conductivity of the foam, which depends on a variety of parameters like temperature range, pore's surface opacity/transparency or reflectivity, and porosity [40]. For an in-depth discussion on the contribution of radiation heat transfer to the effective heat conductivity of cellular materials, readers are referred to Refs. [5,44,45]. Knowing that the thermal conductivity of highly-conductive solids such as metals are generally 10 to 1000 times greater than polymers (e.g. polyurethane foam), for the matrix material, porosity, and temperature ranges considered in this manuscript, the percentage of contribution of radiation is expected to be significantly less than the percentage, mentioned earlier for polyurethane foams. In addition, in this study small size pores are assumed to be empty or filled with less-conductive gases, therefore conductive and convective contributions of the gaseous inclusion are also deemed negligible. As a result, the focus of this manuscript is only on the contribution of the conductivity of the solid materials on the effective thermal conductivity of the porous cellular metamaterials.

3.1. Analytical modelling

Using the analogy between thermal and electric fields, the thermal circuit method with parallel and series configurations is used to derive closed-form expressions for the upper and lower

bounds of the thermal conductivity of cellular materials with rectangular or elliptic inclusion/pore. In this approach, the thermal gradient is analogous to electric voltage, the heat flow represents the electric current, and the thermal resistance, being equal to the reciprocal of thermal conductivity for a unit cell, corresponds to electric resistance [31]. To establish this analytical model, Fig. 4 shows that the unit cell is divided into rectangular elements acting as thermal resistors while the heat flux is considered to flow along the y direction and perfect thermal contact is assumed between the matrix (solid cell walls) and the filler (air for cellular materials).

Using the adopted concept in Fig. 4, closed-form thermal conductivity formulations are derived and presented in Table 3. A detailed sample calculation is provided in supplementary materials S3. In Table 3, k_m and k_i are the thermal conductivity of the matrix and inclusion, respectively. In addition, l is the dimension of the square RVE, a and b are the pore length and width along the x and y directions, respectively; $\lambda_a = a/l$, $\lambda_b = b/l$, $\lambda_k = k_i/k_m (< 1)$, $\theta = \text{atan}(\sqrt{((1 - \lambda_k)\lambda_a)^{-2} - 1})$ and $A = \lambda_b(1/\lambda_k - 1)$. It can be deduced that the Vertical adiabatic lines expressions for both rectangular and elliptic geometries reduce to $K_{yy}^{\text{eff}}/k_m = 1 - \lambda_a$ when $K_i = 0$, which corresponds to cellular materials with empty (vacuum) pores. The relative density of the matrix can be calculated as $(\rho_m)_r = (l^2 - ab)/l^2 = 1 - \lambda_a\lambda_b$ and $(\rho_m)_r = (l^2 - \pi ab/4)/l^2 = 1 - \pi\lambda_a\lambda_b/4$, for cells with rectangular and elliptic inclusions/pores, respectively.

By assuming the origin of the coordinate system at the center of the 2D RVEs with elliptic and rectangular pores, it is evident that these architectures are symmetric about x and y axes. Having one of these geometrical symmetries, there would be no preferences for one side of the symmetric axes to allow more heat to flow. Therefore, the heat transfer along the axes of symmetry is also symmetric. In other word, with a temperature gradient along the axes of symmetry (x or y direction), the effective heat flow normal to the axes is zero. No coupling between temperature gradient in one direction and the heat flux normal to the temperature gradient, is equivalent to zero coupling terms of the thermal conductivity tensor, i.e. the off-diagonal terms of the effective thermal conductivity tensor of the square RVEs with non-rotated elliptic and rectangular pores are zero ($K_{xy}^{\text{eff}} = 0$).

3.2. Computational standard mechanics homogenization

Under the assumption that the RVE of a periodic cellular

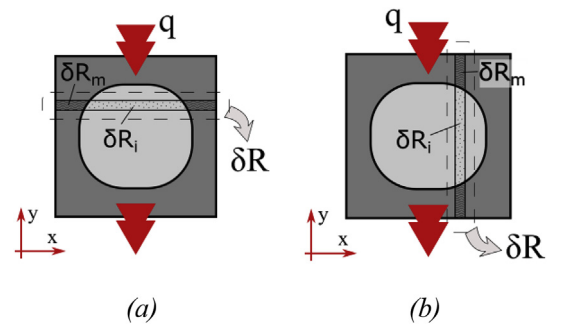


Fig. 4. Schematic view of the thermal resistive elements for: (a) Horizontal isothermal lines where $\delta R^y = \left(\frac{1}{\delta R_m} + \frac{1}{\delta R_i} \right)^{-1}$ and $R^y = \sum \delta R^y$ and (b) Vertical adiabatic lines with $\delta R^y = \delta R_m^y + \delta R_i^y$ and $R^y = \left(\sum \frac{1}{\delta R^y} \right)^{-1}$.

Table 3

Closed-form expressions for K_{yy}^{eff}/K_m of cells made by thermally isotropic and homogeneous matrix and filler material (inclusion), having rectangular and elliptic inclusion/pore shapes, under the assumptions of Horizontal iso-thermal lines or Vertical adiabatic lines.

K_{yy}^{eff}/K_m	Horizontal iso-thermal lines	Vertical adiabatic lines
	$\frac{1 + \lambda_a(\lambda_k - 1)}{1 + \lambda_a(\lambda_k - 1)(1 - \lambda_b)}$	$1 - \frac{\lambda_a \lambda_b (1 - \lambda_k)}{\lambda_k + \lambda_b (1 - \lambda_k)}$
	$\frac{1}{1 - \lambda_b + \frac{\lambda_b}{\lambda_a(1 - \lambda_k)} \left(\frac{\pi - \theta}{\sqrt{1 - ((1 - \lambda_k)\lambda_a)^2}} - \frac{\pi}{2} \right)}$	$\begin{cases} 1 - \lambda_a + \frac{\lambda_a}{A} \left(\frac{\pi}{2} - \frac{\ln(A + \sqrt{A^2 - 1})}{\sqrt{A^2 - 1}} \right), & A > 1 \\ 1 + \lambda_a \left(\frac{\pi}{2} - 2 \right), & A = 1 \\ 1 - \lambda_a + \frac{\lambda_a}{A} \left(\frac{\pi}{2} - \frac{\arctan\left(\frac{\sqrt{1-A^2}}{A}\right)}{\sqrt{1-A^2}} \right), & A < 1 \end{cases}$

material is repeated in all three directions and the RVE is far from the boundaries, the following periodic boundary conditions (Eq. (4)), together with independent unit thermal gradients (Eq. (5)), are adopted on the boundaries [23]:

Periodicity in x direction:

$$T(x_0, y, z) - T(x_0 + l_x, y, z) = l_x \left(\frac{\partial T}{\partial x} \right)_i \quad (4a)$$

Periodicity in y direction:

$$T(x, y_0, z) - T(x, y_0 + l_y, z) = l_y \left(\frac{\partial T}{\partial y} \right)_i \quad (4b)$$

Periodicity in z direction:

$$T(x, y, z_0) - T(x, y, z_0 + l_z) = l_z \left(\frac{\partial T}{\partial z} \right)_i \quad (4c)$$

Independent unit thermal gradients:

$$(\nabla \bar{T})_i = \left(\frac{\partial \bar{T}}{\partial x}, \frac{\partial \bar{T}}{\partial y}, \frac{\partial \bar{T}}{\partial z} \right)_i = \begin{cases} (1, 0, 0), & i=1 \\ (0, 1, 0), & i=2 \\ (0, 0, 1), & i=3 \end{cases} \quad (5)$$

where i is the thermal loading case number and x_0 , y_0 and z_0 are the locations of the three negative faces of the cubic RVE, while l_x , l_y and l_z represent RVE's dimensions along the x , y , and z axes, and $\bar{\nabla}T$ is the average thermal gradient applied to the RVE's boundaries to calculate the microscopic thermal gradients inside the unit cell. Since the RVE is a unit square in 2D analysis and a unit cube in 3D analysis, Eqs. (4) and (5) can be further simplified to:

$$\begin{pmatrix} T(x_0, y, z) - T(x_0 + 1, y, z) \\ T(x, y_0, z) - T(x, y_0 + 1, z) \\ T(x, y, z_0) - T(x, y, z_0 + 1) \end{pmatrix}_i = \begin{pmatrix} 1 \\ 0 \\ 0 \end{pmatrix}_{i=1}, \begin{pmatrix} 0 \\ 1 \\ 0 \end{pmatrix}_{i=2}, \begin{pmatrix} 0 \\ 0 \\ 1 \end{pmatrix}_{i=3} \quad (6)$$

For 2D analysis, all terms in the z dimension are discarded, leading to two independent thermal loading cases. The energy balance equation, i.e. energy equation combined with Fourier heat conduction, is solved over the RVE using the finite element method (FEM). The effective thermal conductivity of the cellular materials

can be calculated by the volumetric averaging of the resultant heat flux based on the standard mechanics homogenization as [46]:

$$\bar{K}_{ij} = \frac{1}{V_{RVE}} \int K_{ik} M_{kj}^T dV_{RVE} \quad (i, j, k = 1, 2, 3) \quad (7)$$

where \bar{K}_{ij} is the effective thermal conductivity tensor, V_{RVE} represents the RVE volume, K_{ik} is the local thermal conductivity tensor, and the M_{kj}^T tensor relates the average and local temperature gradients by $\nabla T = M^T \bar{\nabla}T$.

4. Results and discussion

Starting with verification of the numerical homogenization scheme, the obtained effective thermal conductivities of periodic cubic RVEs with spherical pores in the well-known simple cubic (SC), face-centered cubic (FCC), and body-centered cubic (BCC) arrangements are compared with those found in the literature. Figure S.4 (Supplementary Document) demonstrates the good agreement between our numerical results with those reported in Ref. [47].

To show the effect of filler (inclusion) material on the overall thermal conductivity and to examine the validity of neglecting the thermal conductivity of the gas inside the pore of cellular materials, the homogenized thermal conductivity of a square cell with an empty square pore is benchmarked against the effective thermal conductivity of the same cell filled with air at room temperature. As shown in Fig. 5, for relative densities higher than 10%, the air's thermal conductivity can be neglected without affecting the effective thermal conductivity when the thermal conductivity of the matrix is several orders of magnitude higher than the air, such as in metallic cellular materials.

Under the assumption of neglecting the air, the closed-form expressions presented in Table 3 for the cellular materials with rectangular and elliptic pore topologies are compared with the results obtained by standard mechanics homogenization. As shown in Fig. 6, for all pore's aspect ratios ($\frac{\lambda_a}{\lambda_b} = 1, 2, \text{ and } 3$), the distances between the higher and lower bounds of the effective thermal conductivity of the cells with elliptic pores are larger than those for rectangular pores. Moreover, by increasing the relative density, the

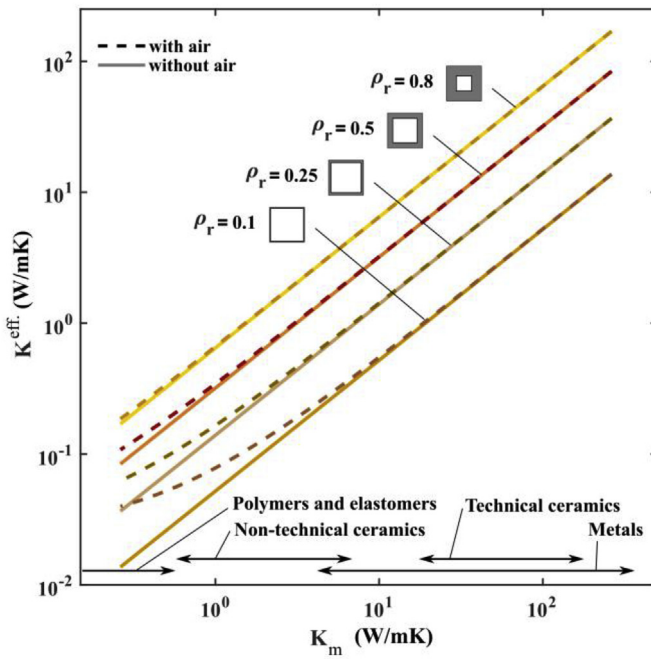


Fig. 5. Effective thermal conductivity of air-filled ($k_{\text{air}} = 0.0263 \text{ W/mK}$) and empty ($k_i = 0$) cellular materials containing a square pore shape versus the thermal conductivity of the solid matrix (log-log scale).

distance between the theoretical bounds increases. In this case, although the pore topology is accounted to derive the theoretical upper and lower bounds, the simplifying assumptions made in deriving the closed-form formula based on the thermal-circuit method make it impossible to accurately predict the effective thermal conductivity.

As shown in Fig. 6, for each pore aspect ratio, cells with rectangular pores exhibit higher thermal conductivities at smaller relative densities. This can be attributed to the minimum wall thickness between the pores. To investigate the role of the

minimum wall thickness on the effective thermal conductivity, parameter λ_t^x is defined as the ratio of the pore distance in x direction with respect to the length of the RVE ($\lambda_t^x = (l - a)/l = 1 - \lambda_a$), which varies between 0 (i.e. connected pore) and 1 (i.e. fully solid material). Defining pore's aspect ratio by $= \lambda_a/\lambda_b$, the λ_t^x parameter can be expressed in terms of the aspect ratio and relative density as:

$$\text{Rectangular pore: } \lambda_t^x = 1 - \sqrt{AR(1 - \rho_r)}, \quad \rho_r > 1 - \frac{1}{AR} \quad (8a)$$

$$\text{Elliptic pore: } \lambda_t^x = 1 - \sqrt{\frac{4AR}{\pi}(1 - \rho_r)}, \quad \rho_r > 1 - \frac{\pi}{4AR} \quad (8b)$$

Using Eqs. (8a) and (8b), the normalized effective thermal conductivity of the 2D cells containing rectangular and elliptic pores are shown in Fig. 7a with respect to the normalized minimum wall thickness. Having the same minimum wall thickness (i.e. the same λ_a), cells with elliptic pores have higher relative density, which indicates that more material is present to transfer the heat through the cellular architecture; as a result, the effective thermal conductivity of cells with elliptic pores, along y direction is higher than cells containing rectangular pores with the same aspect ratio and the same relative wall thickness.

In addition, as can be deduced from Eqs. (8a) and (8b), elliptic pores are wider than rectangular pores at the same relative density. Therefore, for each aspect ratio, minimum relative density (at which pore boundary reaches the boundaries of the RVE) of cells containing rectangular pores is less than those with elliptic pores. Considering the applicable ranges of the relative density in Eqs. (8a) and (8b), for relative densities between $1 - \frac{1}{AR}$ and $1 - \frac{\pi}{4AR}$, cells with horizontal elliptic pores are geometrically inadmissible, while rectangular pores are admissible. As a result, for each pore's aspect ratio, the thermal conductivity curves of the two pore topologies are different at smaller relative densities. In a 2D cellular architecture with elliptic pores, with relative densities slightly greater than $1 - \frac{\pi}{4AR}$, the minimum distance between the pores along x direction is considerably small, making a large thermal resistance

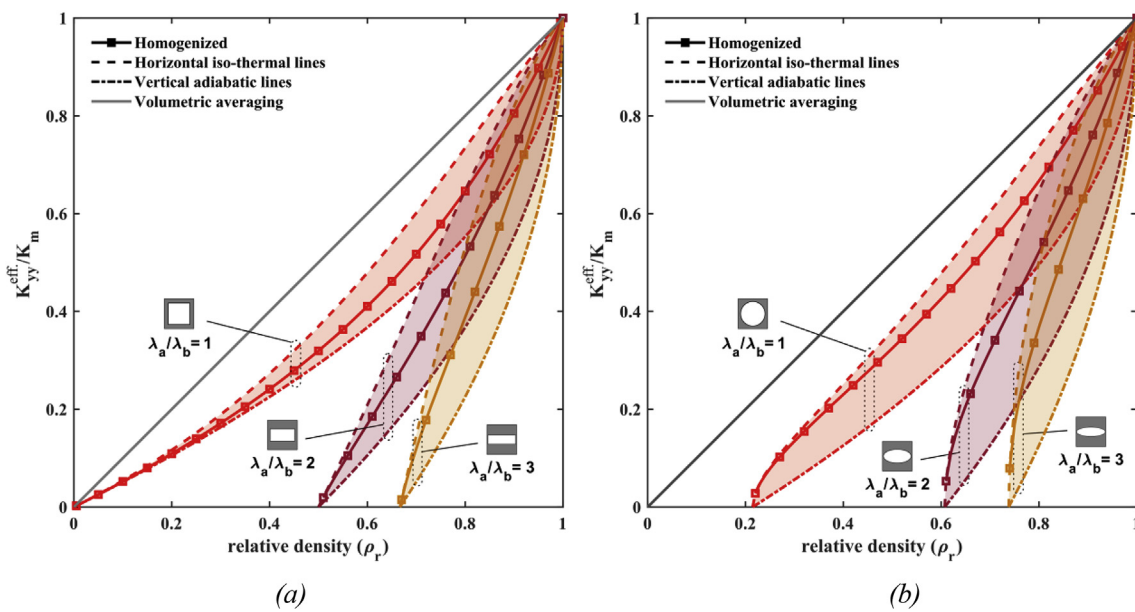


Fig. 6. Theoretical upper and lower bounds along with computational homogenized values of the thermal conductivity in the y direction, normalized by the thermal conductivity of the solid matrix: (a) Rectangular and (b) elliptic pores.

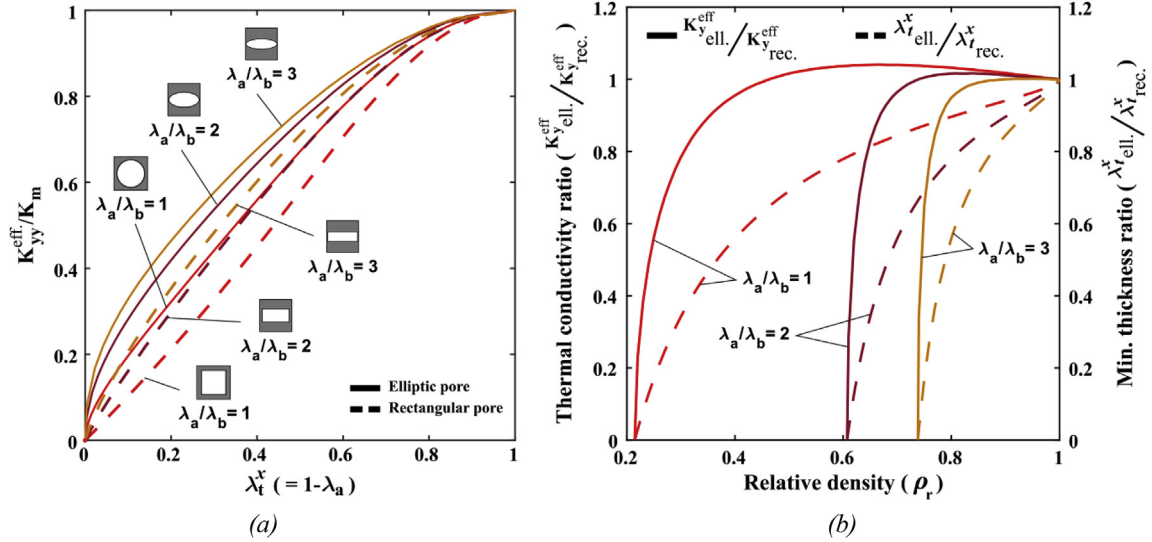


Fig. 7. (a) Effect of minimum distance between pores along x direction on the normalized effective thermal conductivity along y direction for 2D cells with elliptic and square pores and (b) Ratios of the thermal conductivities of these cells, together with the ratios of the minimum wall thicknesses, with respect to relative density.

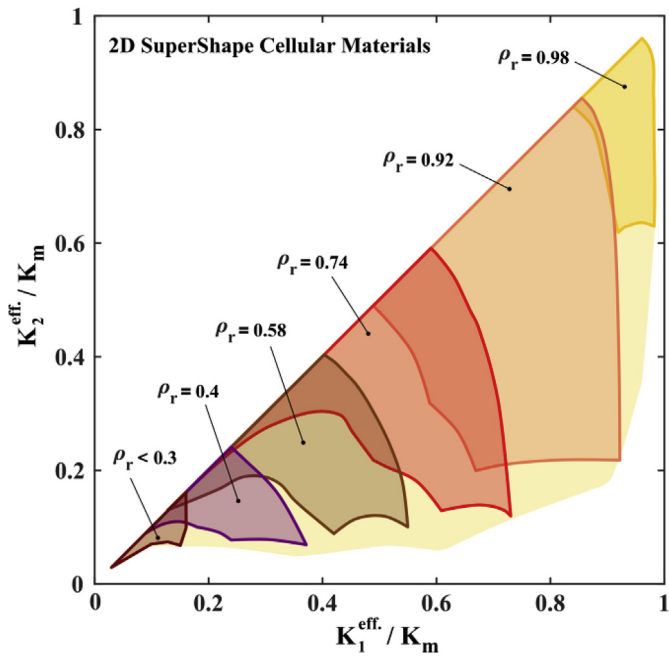


Fig. 8. Normalized effective principal thermal conductivities predicted by standard mechanics homogenization for 2D SuperShape RVEs.



Fig. 9. Two RVEs with relative densities below 0.2, showing isotropic thermal conductivity.

between the pores that significantly decreases the overall heat conductance along the y direction. However, further addition to the relative density increases the minimum wall thickness and provides more space for the heat transfer. In summary, for each pore aspect ratio, at higher relative densities when pore dimensions become notably smaller than the RVE size, the effect of pore shape becomes less important and cells with rectangular and elliptic pores exhibit similar thermal conductivities. This can also be observed in Fig. 7b, where, by increasing the cell's relative density the ratio of the effective thermal conductivity of the two mentioned architectures rapidly increases and remains close to one, for each pore aspect ratio. The ratios of the minimum wall thickness along x direction are also provided in Fig. 7b for comparison.

The standard mechanics homogenization is applied to predict the thermal conductivity of 2D architected cellular metamaterials with SuperShape pore topologies. We consider the variation of the pore's scaling S between 1 and 3.5 (with 0.5 increment) and the pore's rotations in the range of 0° to 90° (with 7.5° increment) to better show the effect of the pore shape and pore rotation on tuning the thermal properties of engineered porous materials. The in-plane effective thermal conductivity generally shows anisotropic properties in x-y coordinate system. As a result, the effective principal thermal conductivities (K_1 as the maximum and K_2 as the minimum) are presented in Fig. 8 instead of K_{xx} , K_{yy} and K_{xy} . Some representative relative densities are highlighted with different colors to show the achievable range of K_1 and K_2 by selected pore

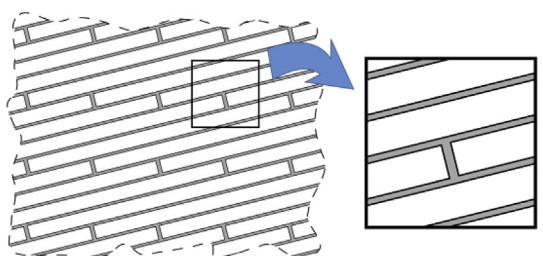


Fig. 10. An example of an RVE with $\rho_r = 0.132$ and a highly anisotropic effective thermal conductivity ($K_1^{\text{eff}}/K_m = 0.122$ and $K_2^{\text{eff}}/K_m = 0.002$). Rectangular pore's specifications are: 19.1 aspect ratio and 14° rotation angle.

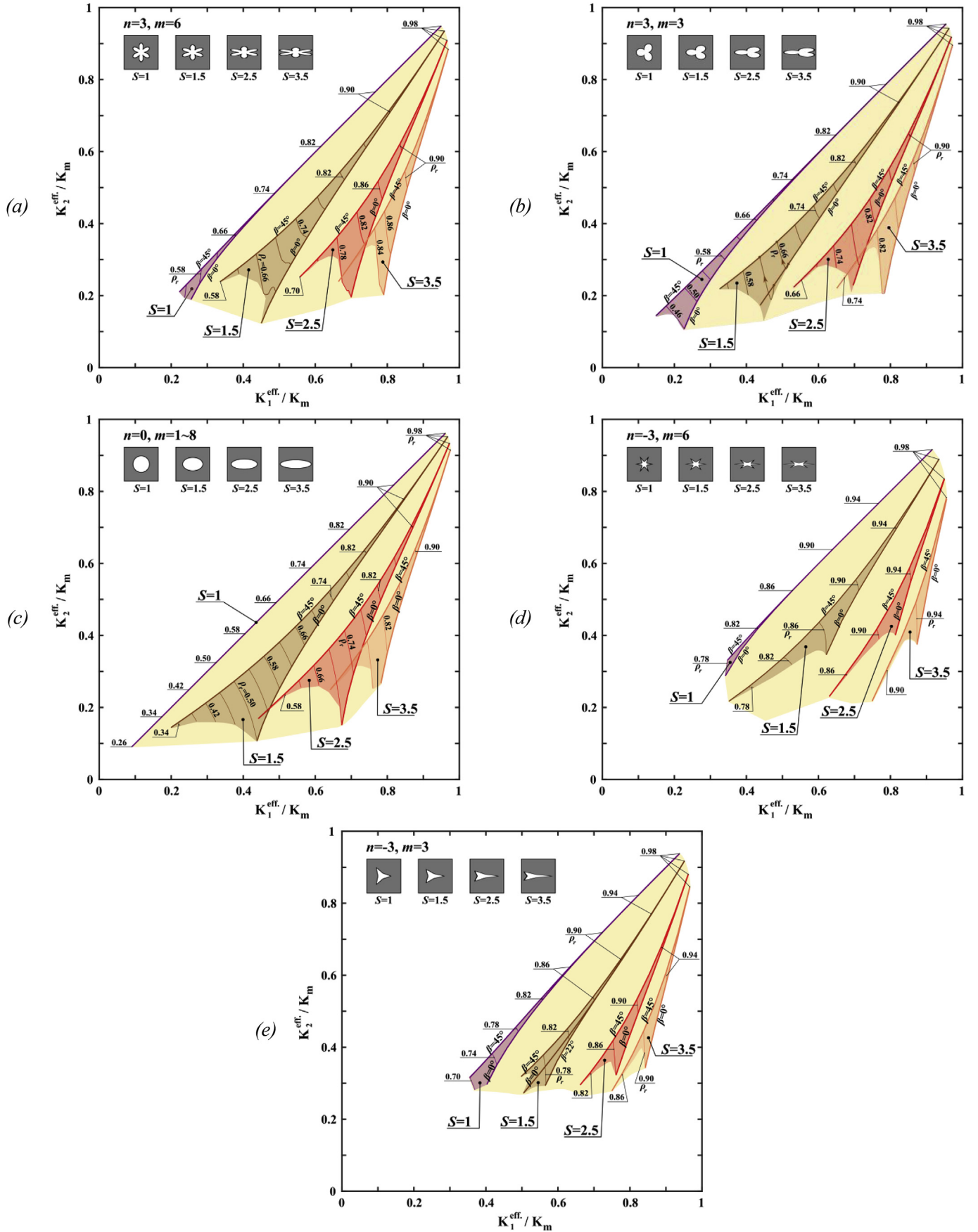


Fig. 11. Effective principal thermal conductivities of 2D Supershape RVEs for different sets of topological parameters: a) $[n = 3, m = 6]$, b) $[n = 3, m = 3]$, c) $n = 0$, d) $[n = -3, m = 6]$, and e) $[n = -3, m = 3]$.

topologies. The large area of K_1 versus K_2 for each relative density allows the engineering of architected cellular materials while keeping the weight constant.

As mentioned earlier, we consider RVEs with enclosed 2D Supershape pores which have wall thicknesses larger than 0.02 times the RVE's length. For this RVE, reducing the relative density pushes the boundaries of the pore towards the cell edges, which makes scaling and rotation impossible at small relative densities. This results in square-like pore topologies with isotropic in-plane effective thermal conductivities for relative densities smaller than 0.2. This behavior can be observed on the far left side of Fig. 8, in which K_1^{eff} and K_2^{eff} are getting closer with decreasing relative density, leading towards thermal isotropy. As an example, Fig. 9 exhibits two RVEs with relative densities below 0.2.

While decreasing the relative density usually leads to isotropic thermal conductivity for square RVEs with a Supershape pore, other cell architectures might enforce anisotropic thermal conductivity even at low relative densities. Fig. 10 shows an example for an RVE which has a pore size several times larger than the RVE's dimensions. While for thermally isotropic materials the ratio of the maximum to minimum principal thermal conductivities is equal to one, the architected cell presented in Fig. 10 exhibits a highly anisotropic effective thermal conductivity, with an in-plane thermal conductivity ratio of $K_1^{\text{eff}} / K_2^{\text{eff}}$ close to 60.

The results presented in Fig. 11 show how the effective thermal conductivity of 2D Supershape cellular metamaterials can be tuned by changing the shape parameters (m, n, S, β and ρ_r) of Supershape pore. A detailed analysis of the results obtained by standard mechanics homogenization, presented in Fig. 11, shows that:

- Narrower relative density range is possible generally with $n < 0$, which is the main reason for the smaller region covered in the K_2^{eff} vs. K_1^{eff} plot for $n < 0$ compared to $n > 0$.
- K_{xy} for all Supershape pore topologies with $\beta = 0^\circ$ is zero, which can be justified by the fact that the defined 2D RVEs (Supershape pore within square cells) are symmetric about the x axis, which in turn makes K_{xy} zero, identifying K_{xx} and K_{yy} as the principal thermal conductivities. Similarly for $\beta = 45^\circ$, the RVEs are symmetric about one of the diagonals of the square cell, thus off-diagonal terms of the conductivity tensor must be zero along this direction.
- With the same relative density, rotating the pore that is elongated in the x direction ($S > 1$) by 45° decreases the $K_1^{\text{eff}} / K_2^{\text{eff}}$ ratio. In other words, rotating the elongated pores and aligning them along the diagonal of the square RVE, reduces the anisotropy of the effective thermal conductivity of the cellular metamaterial. It should be noted that the pore dimensions remain unchanged by keeping the relative density constant. Therefore, rotating the pores by 45° aligns them in the diagonal direction, increasing the distance between the pores of the adjacent cells and providing more space for heat to flow.
- K_1^{eff} and K_2^{eff} of cells with lower pore elongation (S) and higher relative densities are less sensitive to pore rotation than cells with larger S values or cells with smaller relative densities. For instance, for $S = 1.5$ and relative densities above 0.95, pore rotation does not change the principal effective thermal conductivities. However, this is not true for lower relative densities or larger S values.
- Regardless of rotation angle, for $S = 1$, all cases with $m = 4$ or 8 or RVEs with $n = 0$ (circular pore) are thermally isotropic. This is a result of the four-fold rotational symmetry of these Supershape RVEs which leads to $K_{xx}^{\text{eff}} = K_{yy}^{\text{eff}}$ and $K_{xy}^{\text{eff}} = 0$.
- For $m = 2$ and $n > 0$, the Supershape pore is initially elongated in the y direction. For other cases, increasing S generally leads to

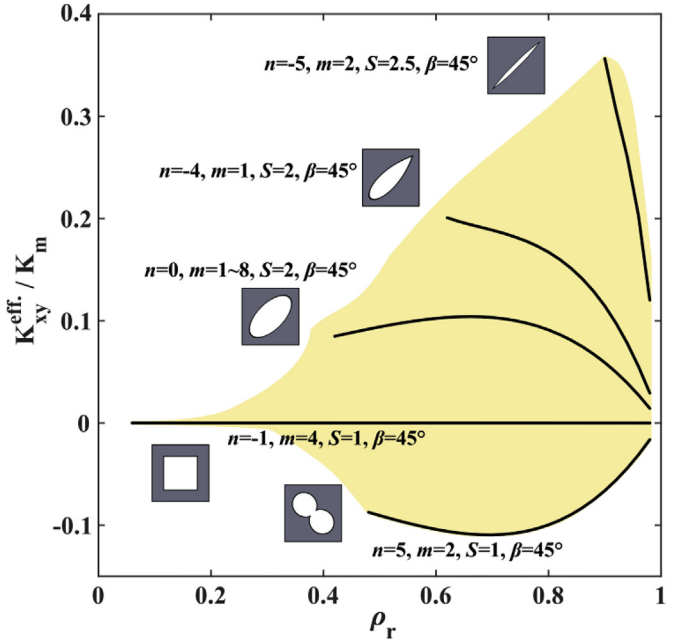


Fig. 12. Effective off-diagonal term in the thermal conductivity tensor for 2D Supershape RVEs with respect to the relative density obtained by standard mechanics homogenization.

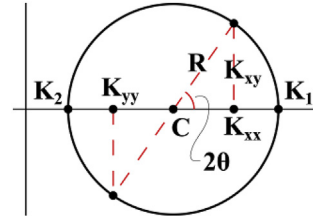


Fig. 13. Using Mohr's circle to calculate the thermal conductivity components for a rotated anisotropic material.

architected metamaterials with highly anisotropic effective thermal conductivity, at the cost of not being able to achieve lower relative densities.

An interesting, but not-widely sought, thermal property of advanced architected materials is off-diagonal terms of the thermal conductivity matrix; i.e. K_{xy} , K_{xz} and K_{yz} . While these off-diagonal terms are zero for thermally isotropic materials and applying temperature gradients in any direction only results in heat flow in that direction, applying temperature gradient along one direction on thermally anisotropic metamaterials can also result in heat flow in other directions. For instance, temperature gradient along the x direction in thermally anisotropic 2D materials (i.e. having non-zero K_{xy}) can also create heat flow in either positive or negative y direction. Fig. 12 shows K_{xy}^{eff} for all analyzed 2D Supershape RVEs with respect to their relative density. Inspecting cases with higher K_{xy}^{eff} shows that highly elongated pores aligned along one of the RVE's diagonals lead to a significant increase of the magnitude of the off-diagonal thermal conductivity term.

It should be noted that by rotating a thermally anisotropic material with respect to a coordinate system, components of its thermal conductivity tensor change; hence, the materials' orientation (not to be confused with pore's rotation) can also be

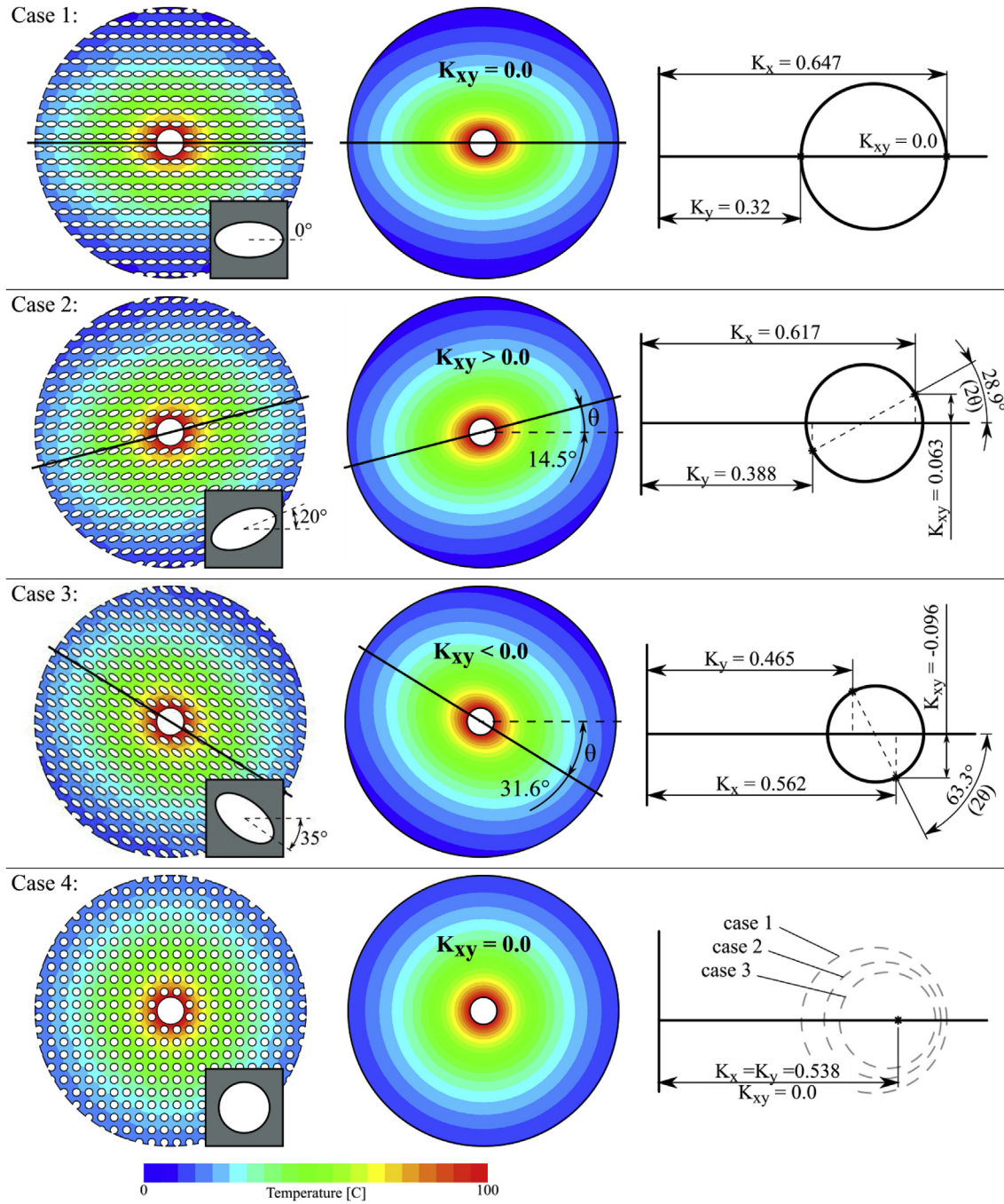


Fig. 14. Effect of changing the pore angle on temperature contours of a cellular disk under thermal loading.

considered as an approach to control the thermal conductivity of an anisotropic material. To obtain the thermal conductivity tensor of the rotated material, coordinate transformation shall be used [7,27], which for 3D materials it can be represented by thermal conductivity ellipsoid, as thoroughly discussed in Ref. [48]. On the other hand, for 2D cases, it is easily shown that the relation between the components of the thermal conductivity tensor (K_x , K_y and K_{xy}) together with the transformation angle (not to be confused with the pore rotation angle), can be demonstrated using Mohr's circle [48,49]. Consequently, to show how K_x , K_y , and K_{xy} of the 2D materials change by rotating the coordinate system and to highlight the effect of the K_{xy} parameter, the Mohr's circle for thermal conductivity, as presented in Fig. 13, is employed. A short discussion on

the use and implications of the Mohr's circle for thermal conductivity is provided in part S5 of the Supplementary document.

To demonstrate the effect of K_{xy} , temperature contours on an annular disk made from different cellular architectures are shown in Fig. 14. The inner and outer diameters are 43 mm and 430 mm, respectively. Temperature at the inner edge is set at 100 °C, the convection coefficient on the outer circle is assumed to be 10 W/m²K with ambient temperature equals to 0 °C, and the thermal conductivity of the hypothetical isotropic solid material is assumed to be 1 W/mK. The 2D square cells with 0.7 relative density, containing elliptic (with pore aspect ratio of 2 and 0°, 20° and -35° pore rotation angles) and circular pores are selected. In addition to the detailed modelling of the porous disks, homogenized disks with

the effective thermal conductivity (obtained by numerical homogenization) are also analyzed with ANSYS Fluent. The observed agreement between the temperature contours of the detailed and homogenized analysis further confirms the validity of the employed numerical simulation.

As shown in Fig. 14, temperature contours in Case 1, 2, and 3 form elliptic shapes, while Case 4 shows a circular temperature contour. To justify that, it is important to note that with the axial symmetry of the disk geometry and the boundary conditions, any distortion in temperature contours can only be attributed to the effective thermal conductivity of the underlying of the cellular metamaterials. If the disk material is thermally isotropic (as in Case 4, a cellular architecture made of square RVEs with circular pores), temperature contours shall also have axial symmetry, which in turn, translates to concentric circular contours. By increasing the anisotropy of the thermal conductivity of the disk, temperature contours become elongated in the direction of higher thermal conductivity (i.e. principal direction). In Case 1, underlying cellular architecture made of cells with horizontal elliptic pores effectively act as a thermally orthotropic material (as discussed earlier, because of geometrical symmetries about x and y axes, K_{xy}^{eff} is necessarily zero in this case) and the principal direction is parallel to x axis. Consequently, temperature contours are elongated in x direction. However for Case 2 and 3, underlying cellular architectures are thermally anisotropic ($K_{xy}^{eff} \neq 0$); hence, temperature contours are elongated in directions other than x or y axis. In Case 2, rotating the pores by 20° makes the value of K_{xy}^{eff} positive. Moreover, from the angle of rotation in the provided Mohr's circle ($2\theta = 29.5^\circ$), it can be inferred that the principal direction is also rotated by 14.5° (counter clockwise), which perfectly match the rotation of the elongated temperature contours. In Case 3, pores are rotated by -35° which makes the value of K_{xy}^{eff} negative and the 2θ angle in the Mohr's circle changes to 63.3° , so the principal direction is rotated by half of this angle, 31.6° , which perfectly matches the rotation of the elongated temperature contours. It is worth noting that similar to what was discussed for the supershape RVEs, rotating the horizontal elliptic pores towards $\pm 45^\circ$ decreases the difference between maximum and minimum effective principal thermal conductivities, which reduces the anisotropy of the material; this can be observed in the Mohr's circle provided for Case 4 in Fig. 14.

As shown here, positive or negative K_{xy} component of the thermal conductivity tensor only describe the direction in which the material shall be rotated to align its direction of principal thermal conductivity with the coordinate system. While K_{xy} can be negative, zero or positive, K_{xx} , K_{yy} and the minimum principal thermal conductivity are all positive in the context of this manuscript.

The application of implementing thermally anisotropic metamaterials to control and manipulate conductive heat flux has been the subject of a number of recent studies [50–53]. Similarly, as the examples in Fig. 14 show, thermally anisotropic cellular architectures can be used to tune the thermal anisotropy of the metamaterials to consequently control the heat flow.

So far, it has been shown that by introducing pores to an isotropic solid material, it is possible to design an architected cellular metamaterial with anisotropic effective thermal conductivity. Fig. 15 shows the possibility of doing the opposite (i.e. creating thermally isotropic cellular metamaterials out of an anisotropic solid material) by introducing elliptic pores similar to Case 1 of Fig. 14, to a disk made by a hypothetical thermally anisotropic solid material with minimum and maximum principal thermal conductivities of 0.43 W/mK (in x -direction) and 1 W/mK

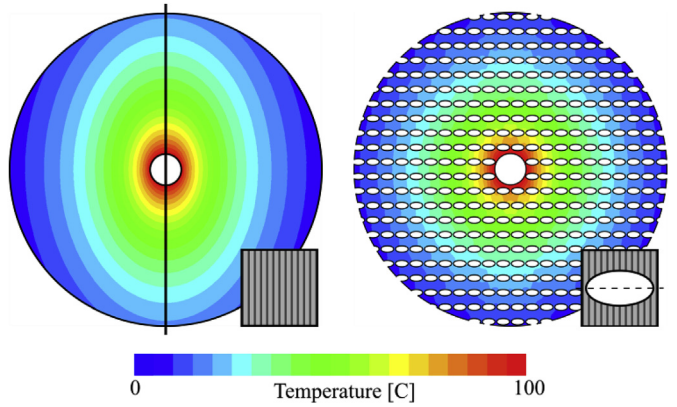


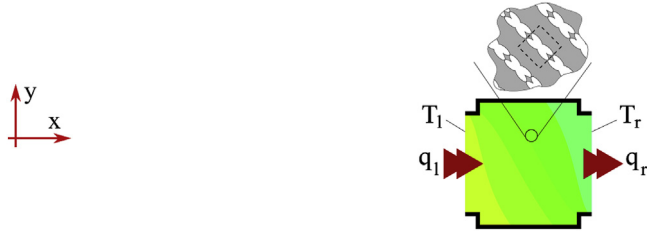
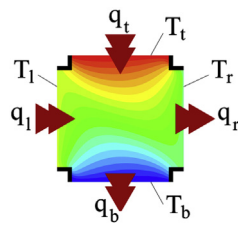
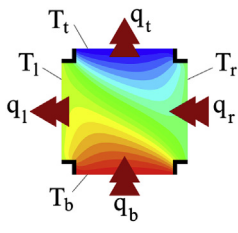
Fig. 15. Temperature contours for a disk made of anisotropic solid material, under thermal loading, before and after introduction of pores.

(in y -direction). While elongated temperature contour on the solid disk in Fig. 15 clearly shows the orthotropy of the base material, the circular-shape temperature contour of the cellular disk can be interpreted as isotropic effective thermal conductivity of the architected cellular disc. Effective thermal conductivity of the RVE of the cellular disk, made of the hypothetical thermally anisotropic solid material, is also obtained by numerical homogenization, which shows that $K_{xx}^{eff} = K_{yy}^{eff} = 0.283$ and $K_{xy}^{eff} = 0$, confirming the possibility of transforming an anisotropic solid material to thermally isotropic materials by appropriate introduction of pores.

High K_{xy} values open up the possibility of controlling the net heat flow in the x direction by tuning the temperature gradient in the y direction. Table 4 presents a case study where the net heat flow in the x direction has been increased (Case b) or reversed (Case c) by applying different temperature gradients along the y direction of a cellular medium made of a -45° rotated Supershape RVE with [$n = 2$, $m = 4$, $S = 2.5$, $\beta = 0$, $\rho_r = 0.68$]. The cellular part is a unit square with its corners cut by 0.1 m , while the thermal conductivity of the thermally isotropic base material is assumed to be 100 W/mK , with the aforementioned architecture, the effective thermal conductivity of the cellular medium is determined as: $K_{xx} = K_{yy} = 37.2 \text{ W/mK}$ and $K_{xy} = -26.8 \text{ W/mK}$. For all cases, the left wall's temperature (T_l) is set at 6°C , while the temperature of the right wall (T_r) is 4°C . In Case a, all the walls are insulated ($q = 0$) except the left and right walls. Positive temperature difference in the y direction is applied in Case b by setting the top wall's temperature (T_t) at 10°C and the bottom wall's temperature (T_b) at 0°C . In Case c, the top and bottom wall temperatures of Case b are swapped so that the temperature difference applied in the y direction is negative. Steady-state heat conduction simulation is conducted using ANSYS Fluent and temperature distribution, together with the effective heat flux passing through the left (q_l), right (q_r), top (q_t) and bottom (q_b) walls of the part are presented in Table 4, in which as of convention, positive sign for heat flux stands for inward and negative sign indicates outward heat fluxes. The observed coupling between the heat fluxes in both x and y directions in Case b and Case c, which is caused by the non-zero K_{xy} , highlights the importance of the off-diagonal components of the thermal conductivity tensor. Failing to consider this coupling might result in completely different temperature distribution and inaccurate conclusions. For instance, in Case c although the imposed temperature difference in the x direction is negative, the apparent heat flow in this direction is also negative. Referring to Eq. (3), this leads to deducing a negative thermal conductivity for the cellular part, if the aforementioned coupling is ignored.

Table 4

Thermal response of a square cellular part made by an anisotropic cellular architecture, subjected to a negative temperature gradient in the x direction ($T_l > T_r$) and different boundary conditions in the y direction. Thick solid black lines represent insulated walls.

	Case a	Case b	Case c
			
			
			
Boundary Conditions	$T_l = 6^\circ\text{C}$, $T_r = 4^\circ\text{C}$, $q_b = q_t = 0 \text{ W/m}^2$	$T_l = 6^\circ\text{C}$, $T_r = 4^\circ\text{C}$, $T_b = 0^\circ\text{C}$, $T_t = 10^\circ\text{C}$	$T_l = 6^\circ\text{C}$, $T_r = 4^\circ\text{C}$, $T_b = 10^\circ\text{C}$, $T_t = 0^\circ\text{C}$
Inward and outward heat fluxes [W/m²]	$q_l = 43.2$, $q_r = -43.2$	$q_l = 280.2$, $q_r = -280.2$, $q_b = -429.2$, $q_t = 429.2$	$q_l = -123.9$, $q_r = 123.9$, $q_b = 349$, $q_t = -349$

As shown in Fig. 16, by adding a small thickness to 2D Supershape RVEs and assembling them in a predefined 3D arrangement, thin-walled open lattices are introduced in this paper. Using a finite element simulation in ANSYS APDL to conduct standard mechanics homogenization, effective thermal conductivity of these lightweight 3D architected RVEs is then determined.

To show the influence of pore topology of one side on the heat flow through the other sides of the thin-walled RVE, a simple mathematical model is derived based on superposition, in which heat flow through different RVE sides is assumed independent, and any heat flow or thermal resistance normal to all sides are neglected. Under these assumptions, all six RVE sides can be treated as separate entities as depicted in Fig. 16. Consequently, the effective thermal conductivity can be determined by summing up the contributions of these individual sides. Assuming that the effective in-plane thermal conductivities of the faces of the 3D RVE (which are 2D Supershape RVEs) in their 2D local coordinate systems are given by $K_{zx\text{ face}}^{\text{eff}} / K_m = \begin{bmatrix} a3 & c3 \\ c3 & b3 \end{bmatrix}_{\text{local}}$, $K_{yz\text{ face}}^{\text{eff}} / K_m = \begin{bmatrix} a2 & c2 \\ c2 & b2 \end{bmatrix}_{\text{local}}$, and $K_{xy\text{ face}}^{\text{eff}} / K_m = \begin{bmatrix} a1 & c1 \\ c1 & b1 \end{bmatrix}_{\text{local}}$, the overall thermal conductivity of the 3D thin-walled open RVE is calculated as:

$$K_{3D}^{\text{eff}} / K_m \approx t_r \begin{bmatrix} a1 + b3 & c1 & c3 \\ c1 & b1 + a2 & c2 \\ c3 & c2 & a3 + b2 \end{bmatrix} \quad (9)$$

where the relative wall thickness t_r is defined as the total wall

thickness divided by RVE's length. Since the same pore topologies are applied to all sides of the thin-walled RVE, Eq. (9) can be further simplified as:

$$K_{3D}^{\text{eff}} / K_m \approx t_r \begin{bmatrix} a1 + b1 & c1 & c1 \\ c1 & b1 + a1 & c1 \\ c1 & c1 & a1 + b1 \end{bmatrix} \quad (10)$$

This equation satisfies $K_{xx} = K_{yy} = K_{zz}$ and $K_{xy} = K_{yz} = K_{zx}$ for the introduced thin-walled RVEs, which arise from their three-fold rotational symmetry about their diagonals. Equation (10) also predicts a linear relation between the relative wall thickness and the effective thermal conductivity. Fig. 17 compares the prediction of Eq. (10) with the results of 3D standard mechanics homogenization for some of the thin-walled RVEs. Since the discrepancies between the aforementioned methods are highest for 0.1 relative wall thickness, the homogenization results for other relative thicknesses are not presented. As shown in Fig. 17, the predicted results by Eq. (10) show good agreement with the 3D homogenization. However, because the heat flow and thermal resistance normal to each RVE face were neglected, small K_{xx} overprediction can be seen as if the results are slightly shifted to the right.

Although the superposition-based model shows good agreements with 3D standard mechanics homogenization, because it does not account for the influences of pore geometry of one face on the heat flow through the other faces, its prediction of the effective thermal conductivity of thin-walled open lattices might deviate noticeably from the 3D homogenization. An example is provided in

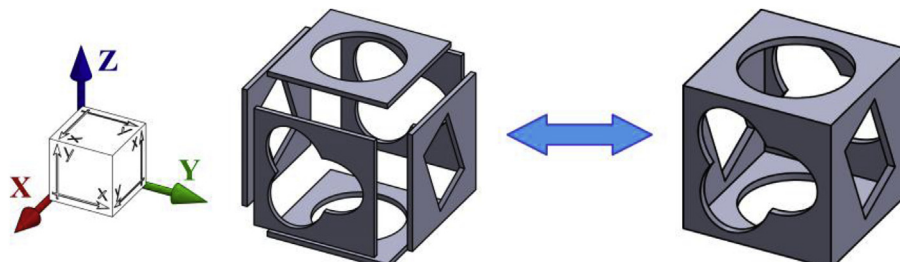


Fig. 16. Assembling or disassembling a general thin-walled open lattice RVE.

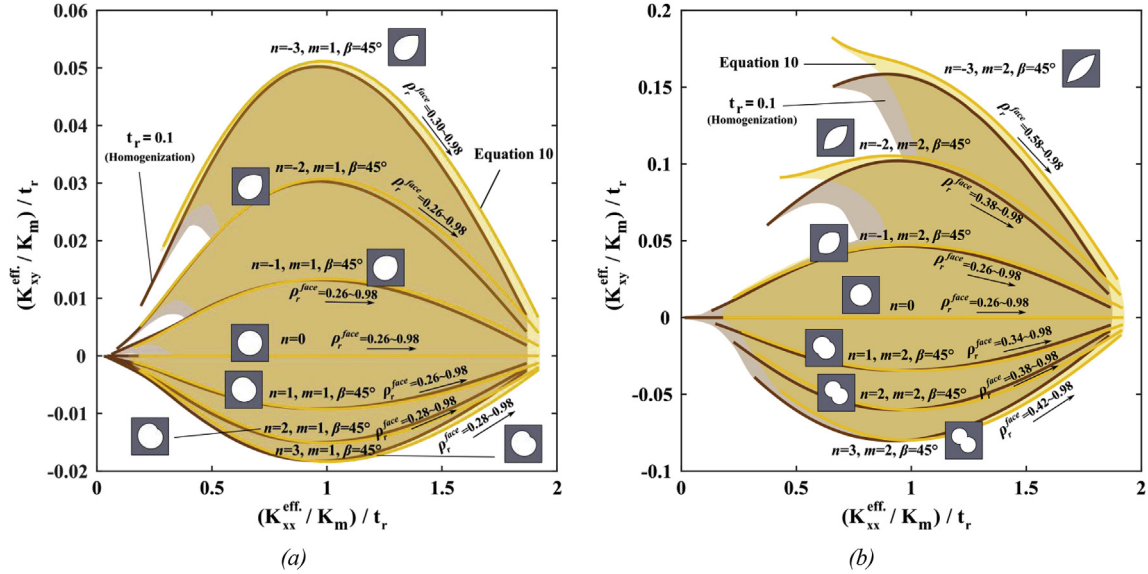


Fig. 17. Effective K_{xx} and K_{xy} normalized by the base material's thermal conductivity times the relative wall thickness, for the thin-walled open lattices based on: (a) Supershape parameter $m = 1$ and (b) Supershape parameter $m = 2$. Only the face of the 3D RVE in the x-y plane is shown.

Fig. 18, in which Eq. (10) predicts zero effective K_{xy} , while the actual value of this parameter changes with the relative density of 3D RVE for a Supershape parameter set as $[n = -3, m = 3, S = 1, \beta = 0]$. It should be noted that the assumptions made to neglect the heat transfer mechanisms other than conduction inside the matrix might lose their validity for lower relative densities of thin-walled open-cell lattices.

To show the versatility of the achievable effective thermal conductivity of thin-walled open lattices, the thermal conductivity of P, D and G shellular materials are compared. The computational analysis shows that unlike most of the considered 2D and 3D architected cellular metamaterials, P, D and G shellular materials

are thermally isotropic and thus only one value is reported in Figs. 19 and 20. The P, D and G shellular materials (when $f = 0$) show almost equal thermal conductivity at each relative density, a phenomenon that is in agreement with the findings reported elsewhere [26]. Curve fittings of the effective thermal conductivities of these shellular materials are provided in Table 5 (with the coefficient of determination $R^2 > 0.9999$). As the power-law exponents for the relative density are all close to unity, it can be inferred that for relative densities below 0.25, the thermal conductivity of G, D and P shellular materials varies almost linearly with relative density. Relative density of the aforementioned shellular architecture are provided in Table 2.

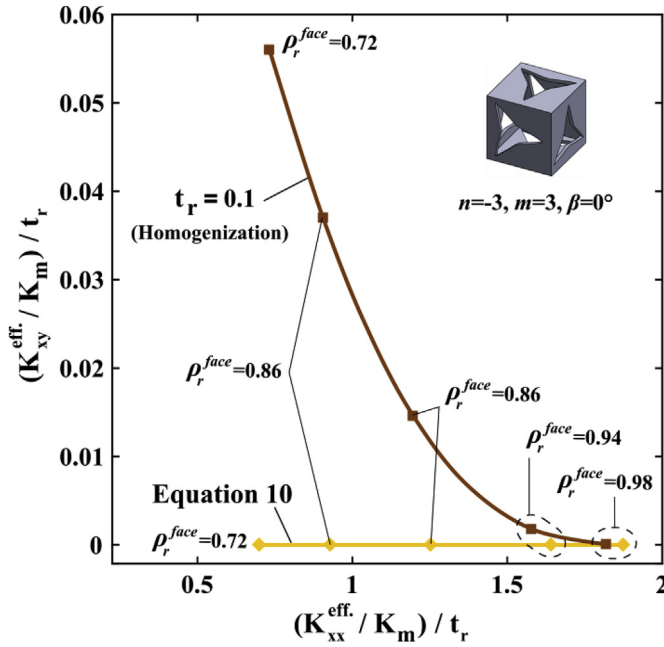


Fig. 18. Deviation of the results of Eq. (10) from 3D standard mechanics homogenization for thin-walled open lattice with Supershape parameters set as $[n = -3, m = 3, S = 1, \beta = 0]$.

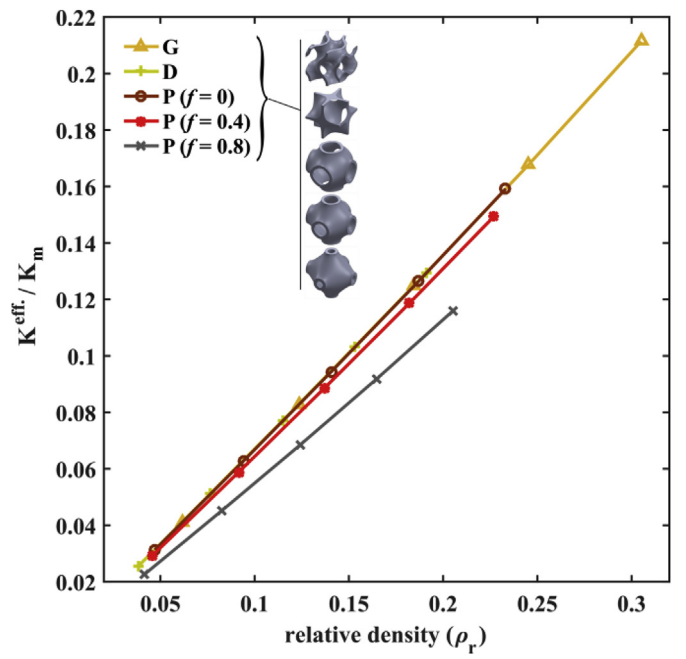


Fig. 19. Effective thermal conductivity of shellular materials, normalized by thermal conductivity of the solid matrix, with respect to relative density.

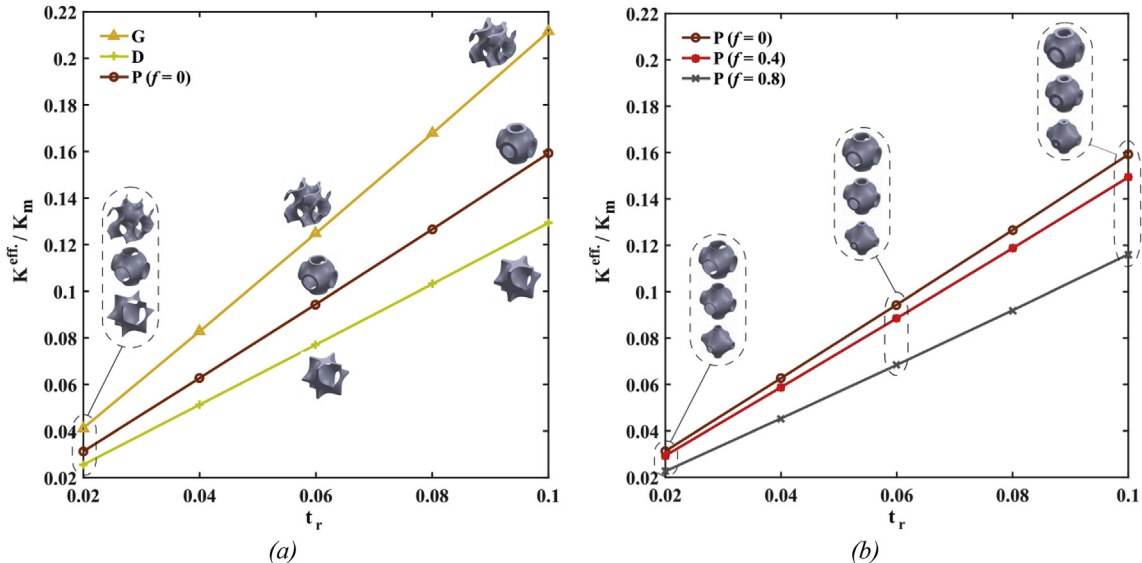


Fig. 20. Normalized effective thermal conductivity of shellular materials with respect to relative thickness: (a) G, D and P shellular materials with $f=0$, and (b) P shellular materials with different f values.

Table 5

Curve fittings of the normalized effective thermal conductivity of P, D and G shellular materials in the form of $K_{\text{eff}}/K_m = C_0 (\rho_r)^n$.

$G (f=0)$	$D (f=0)$	P family	$f=0$	$f=0.4$	$f=0.8$
$0.7060 (\rho_r)^{1.0219}$	$0.6853 (\rho_r)^{1.0089}$	$0.6941 (\rho_r)^{1.015}$	$0.6700 (\rho_r)^{1.0157}$	$0.5808 (\rho_r)^{1.0219}$	

Fig. 20a shows the normalized effective thermal conductivity of P, D and G shellular materials (with $f=0$) with respect to their relative wall thickness. As shown in this figure, for the same relative thickness, type G has the highest thermal conductivity among the three shellular materials, while type D has the lowest thermal conductivity. As provided in Table 2, at the same relative thickness, type G shellular materials have the highest relative density among the three shellular materials. Since relative density is one of the most influential parameters on the effective thermal conductivity, it is then reasonable for the type G shellular material to have a higher effective thermal conductivity than P and D shellular materials with the similar relative thickness. With the same logic, as type D shellular architectures have the lowest relative density for the same relative thickness, its effective thermal conductivity is smaller than the other shellular materials considered here. The effect of f parameter on the overall thermal conductivity of type P shellular materials is also examined. As shown in Figs. 19 and 20b, for the same relative density or the same relative thickness, increasing f decreases the effective thermal conductivity of type P shellular materials. This can be justified by the change in the spatial distribution of the material inside each cell. In other words, when $f=0$, more material is involved in the effective heat transfer throughout the shellular medium compared to $f=0.8$.

Fig. 21 presents the plots of $K_1^{\text{eff}} - K_2^{\text{eff}}$ for all 2D and 3D RVEs introduced in this paper. To compare the thermal conductivity of the 2D Supershape, 3D thin-walled open lattices, and selected shellular materials, K_1^{eff} and K_2^{eff} were selected as the maximum and minimum principal effective thermal conductivity, respectively. It should be mentioned that for a 3D RVE made by thickening of a 2D Supershape RVE, the effective out-of-plane thermal conductivity (K_{zz}) follows the rule of mixtures since there is no topological

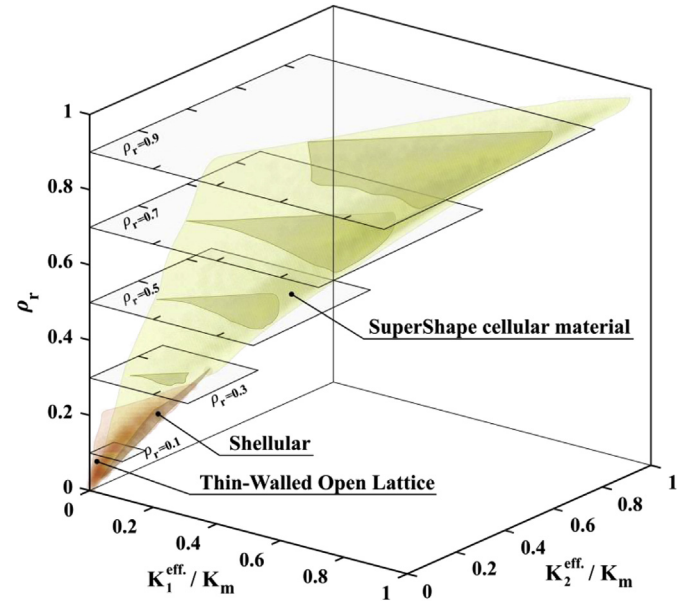


Fig. 21. Maximum vs. minimum effective principal thermal conductivity of 2D Supershape cellular material, 3D thin-walled open lattices, and shellular materials for different relative densities.

change or heat transfer obstruction through the thickness. The relation between K_1^{eff} , K_2^{eff} and K_3^{eff} for thin-walled open lattices with different m and n values is presented in supplementary document part S6 (Fig. S.6).

Using a *MarkerBot Z18*, a fused deposition modelling (FDM) 3D

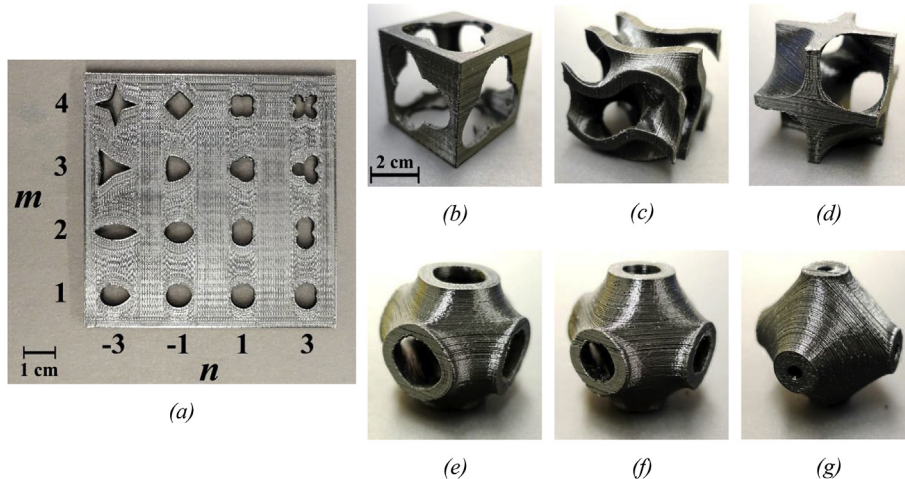


Fig. 22. FDM 3D printed unit cells of some 2D and 3D RVEs presented in this paper: (a) 2D Supershape RVEs, (b) Thin-walled open lattice, (c) Gyroid or G shellular ($f=0$), (d) Diamond or D shellular ($f=0$), (e) Primitive or P shellular with $f=0$, (f) P shellular with $f=0.4$ and (g) P shellular with $f=0.8$. All 3D RVEs are $4 \times 4 \times 4 \text{ cm}^3$.

printer, the manufacturability of the architected cellular metamaterials is verified. Fig. 22 shows representative 3D printed unit cells made by layer-by-layer deposition of molten polylactic acid (PLA) using a 0.4 mm nozzle size, layer thickness around 0.1 mm and with 3D support structures where the part has overhang beyond 65° . While Fig. 22 confirms FDM 3D printing as a possible manufacturing process to produce cellular metamaterials, more precise additive manufacturing techniques, like stereolithography (SLA) or selective laser sintering (SLS), can be considered to reduce the manufacturing defects for the production of architected metamaterials.

This manuscript focuses on the theoretical aspects of thermal conductivity in architected cellular metamaterials. While the experimental characterization aspects of these cellular metamaterials are out of the scope of the current study and require a separate investigation, readers may refer to references [54–58] for considerations on the steady state or transient techniques for experimental thermal characterization of these metamaterials.

5. Functionally graded cellular materials

To explore the effect of tailoring the pore architecture across the cellular metamaterials on tuning the heat flow, topology and cell relative density of Supershape pores can be graded according to the concept of *functionally graded cellular materials* (FGCMs) [59,60]. Functionally graded materials (FGMs) are inhomogeneous media in which material properties gradually change with respect to location. In the case of FGCMs, micro-architectural parameter of cells, such as relative density, pore shape, pore elongation, and pore rotation, spatially varies throughout the material to optimize the cellular media for specific thermal or mechanical requirements [61]. Among all the possibilities, only the effect of pore rotation angle variation on the heat flux and temperature distribution is investigated here. Specific cell arrangements with similar pore shape but with different rotation angles are investigated to maximize or minimize the heat flow passing through the top (Q_t) and right (Q_r) edges of the cellular media while controlling the maximum temperature (T_{\max}) within these advanced cellular metamaterials.

As illustrated in Fig. 23, a $1 \text{ m} \times 1 \text{ m}$ 2D architected FGCM, consisting of 10×10 cells with empty pores, is considered and 100 W heat is applied on the left side which leaves the cellular medium from the top, right, and bottom edges through heat

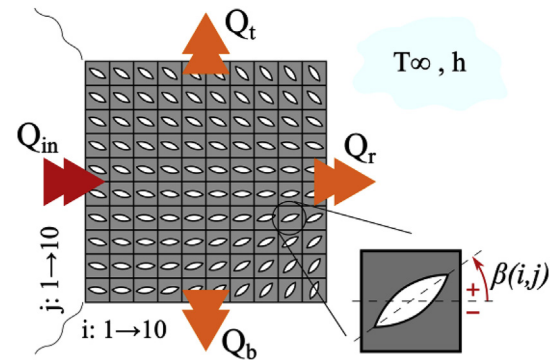


Fig. 23. Schematic representation of an FGCM subjected to thermal loading.

convection with an ambient temperature of 0°C and a heat convection coefficient of $1 \text{ W/m}^2\text{K}$ (close to free convection in dry air). The base material of the FGCM is assumed isotropic with a thermal conductivity of 1 W/mK (such as some non-technical ceramics). The topology of the empty pores within the FGCM is formed by the following sets of parameters in the Supershape formula: $n = -2$, $m = 2$, $S = 1.5$, $\rho_r = 0.8$. The pore angles of rotation at the four corners of the FGCM medium ($\beta(1,1)$, $\beta(1,10)$, $\beta(10,1)$ and $\beta(10,10)$, equal to β_1 , β_2 , β_3 , and β_4 respectively) are independently tailored between -90° to 90° with $\Delta\beta_i = 22.5^\circ$. The rotation angle of the pores within the FGCM is linearly interpolated by:

$$\begin{aligned} \beta(i,j) &= \frac{\beta_4 - \beta_3 - \beta_2 + \beta_1}{(n_y - 1)(n_x - 1)} (i - 1)(j - 1) + \frac{\beta_3 - \beta_1}{(n_x - 1)} (i - 1) \\ &\quad + \frac{\beta_2 - \beta_1}{(n_y - 1)} (j - 1) + \beta_1 \\ &\quad (1 \leq i \leq n_x, 1 \leq j \leq n_y) \end{aligned} \quad (11)$$

where n_x and n_y are the number of cells in the x and y directions, respectively. Here, $n_x = n_y = 10$.

The numerical results for the heat flux at the top (Q_t) and right (Q_r) edges, as well as the maximum temperature within the FGCM (T_{\max}), are illustrated in Fig. 24a, b and 24c, respectively. As a side note, nine cases exist where all the pores have the same rotation angle within the medium, representing periodic architected cellular materials that are not graded. Numerical results for these

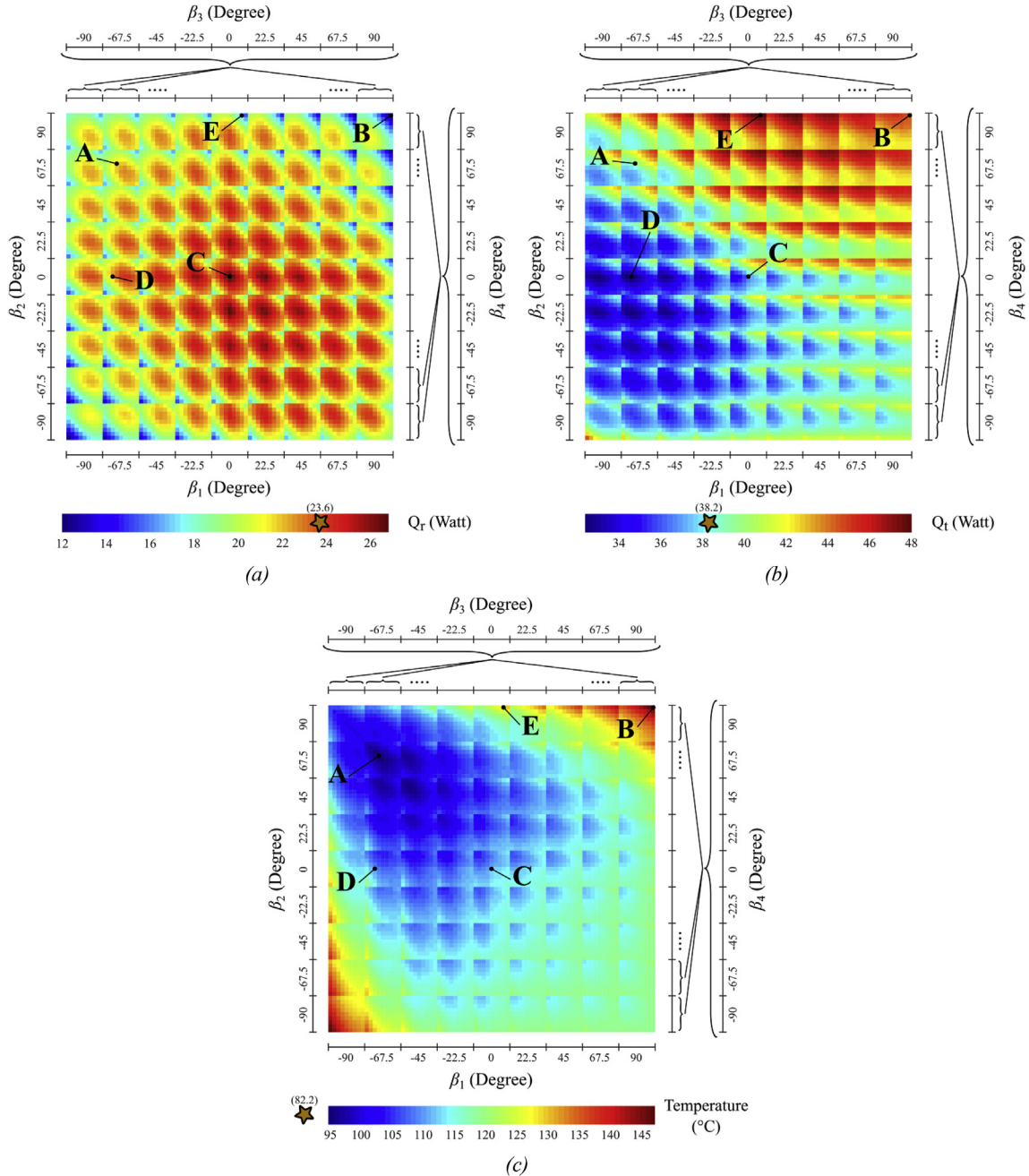


Fig. 24. Numerical simulation results of the square FGCM introduced in Fig. 23 for different β_1 to β_4 values. (a) Heat flow rate through the right edge (Q_r), (b) Heat flow rate through the top edge (Q_t), and (c) Maximum temperature throughout the FGCM. Stars on the color bars indicates Q_r , Q_t and T_{max} for the solid part under the same boundary conditions. For points A-E, please refer to Table 6. (For interpretation of the references to color in this figure legend, the reader is referred to the Web version of this article.)

architected cellular cases are also separately presented in Fig. 25.

Within the FGCM each empty pore can be considered as a wall guiding the heat to flow along its elongation direction, preventing it from transferring in the normal direction. Using this analogy, having all pores with zero rotation angle ($\beta_1 = \beta_2 = \beta_3 = \beta_4 = 0^\circ$) would guide more heat towards the right edge creating the case having maximum Q_r (point C in Fig. 24). Similarly, when all the pores are 90° rotated ($\beta_1 = \beta_2 = \beta_3 = \beta_4 = 90^\circ$ or -90°), more heat is being blocked from going towards the right side resulting in the minimum Q_r (point B in Fig. 24). For these two cases, the FGCM is symmetric about the x axis. Therefore, as Q_t and Q_b are equal, they do not correspond to minimum and maximum Q_r ; but correspond

to the minimum and maximum of $Q_t + Q_b$ (which is equal to $100 - Q_r$). In other words, to maximize Q_t instead of minimizing Q_r , summation of Q_r and Q_b shall be minimized. This can be achieved by arranging the pores in directions that maximize the heat flow towards the top edge, while minimizing it in the other two directions. Points E and D in Fig. 24 represent the maximum and minimum achievable Q_r . Introducing voids (or pores) into a solid media decreases its local thermal conductivity, which in turn translates into an increase in the maximum temperature. To control the increased maximum temperature, heat should encounter minimum resistance in its flowing direction towards the top, right and bottom edges. The functionally graded cellular arrangement

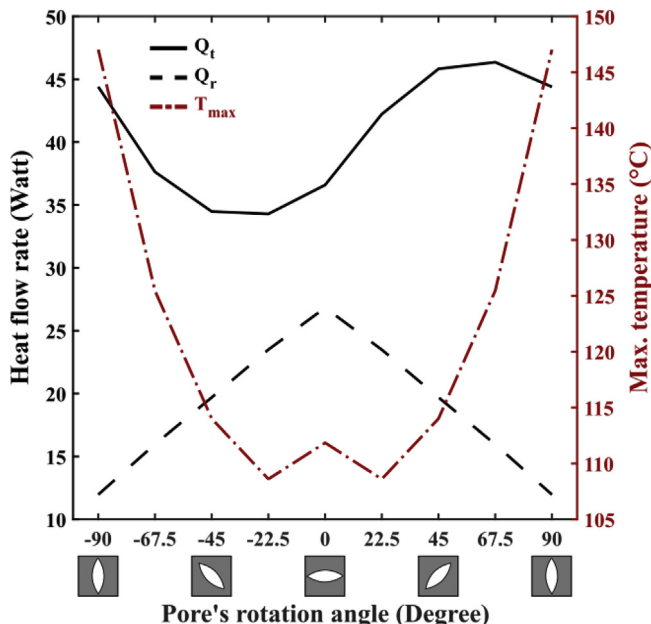


Fig. 25. Heat flow rates through the top and right edges together with the maximum temperature as a function of pore's rotation angle, in the part made by uniform cellular materials ($\beta_1 = \beta_2 = \beta_3 = \beta_4$).

corresponding to the minimum increase in T_{max} is indicated by point A in Fig. 24. Results for points A to E are summarized in Table 6.

To demonstrate how tailoring the pore topology can tune the thermal performance of architected cellular media, numerical thermal results are compared with a corresponding fully solid medium. It can be seen that while the weight of both functionally graded and uniform cellular media is 20% lower than their solid counterparts, Q_t can be increased by more than 25% using graded pore angles, compared to a 21% increase achievable by uniform cellular materials. As presented in Table 6, when minimizing the heat flux through the top edge of a cellular medium is of design interests, using an appropriate FGCM makes it possible to decrease Q_t by 15%, while a uniform cellular material can only reduce Q_t by at most 10%. In addition, it is possible to limit the unavoidable rise of the maximum temperature within the architected cellular medium and have T_{max} equal to 115% of those of the solid medium value using the graded pore angles, while for uniform cellular media minimum T_{max} is 32% higher than the solid medium.

This section focused on the effect of grading pore rotation angles

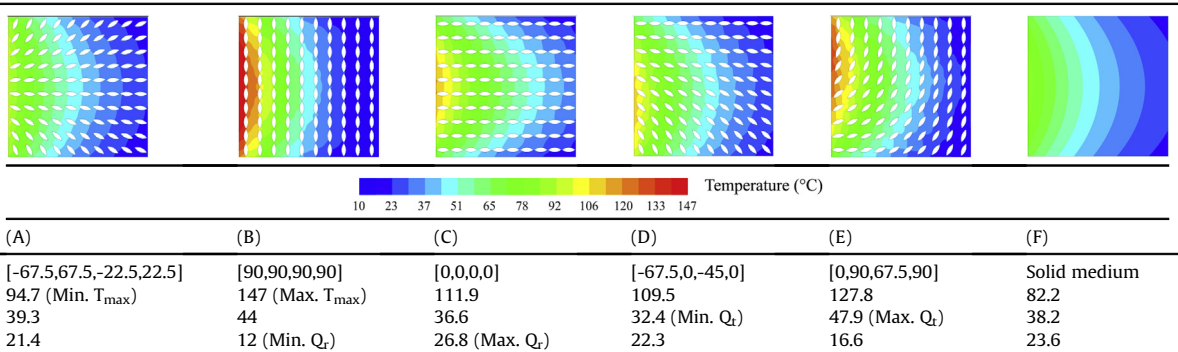
throughout an FGCM on the heat flow and temperature distribution inside the material to show the advantages that architected FGCMs can offer for designing advanced materials to control/tune heat flow in desired directions and limiting the maximum temperature within cellular media. For structural applications of architected cellular metamaterials where thermal and mechanical properties are both crucial, in addition to the pore's rotation angle, other topological parameters of the cell microarchitecture (e.g. pore topology, relative density, elongation and even material composition) can also be spatially tailored throughout the FGCMs to achieve the highest multifunctional efficiency, for example in lightweight, structurally durable and highly-efficient thermal insulators.

6. Concluding remarks

Theoretical and computational methodologies have been conducted in this paper for predicting the effective thermal conductivity of architected cellular metamaterials. We firstly examine the validity of neglecting the thermal conductivity of air inside the pores of cellular materials by determining their effective thermal conductivity using derived closed-form expressions and numerical homogenization. We then used computational prediction of standard mechanics homogenization for analyzing the effect of cell microarchitecture on effective thermal conductivity of 2D cellular metamaterials with Supershape pore architectures of different pore shape, scaling and rotations. The results presented a wide range of achievable anisotropic effective thermal conductivity for different relative densities. While the results in this paper and in the available literature are mostly focused either on the effective thermal conductivity in the x and y directions, or the effective principal conductivities, we also explored the importance of off-diagonal terms in the thermal conductivity tensor using a case study. Then, the thermal conductivity of novel lightweight thin-walled open lattices, introduced based on 2D Supershape pores, was examined. A mathematical model based on superposition was derived to calculate the effective thermal conductivity of thin-walled open lattices using the properties of 2D cellular materials with Supershape pores. Comparing the predictions of this model with the numerical homogenization revealed that pores of one side of the cell alters the heat transfer through the other sides, further highlighting the importance of the cell architecture on the effective thermal conductivity of cellular materials. Different TPMS-based shellular lightweight materials were also analyzed to compare their thermal conductivity with those of thin-walled open lattices. For the range of relative density investigated ($\rho_r < 25\%$), G, D and P shellular materials with $f=0$ were found to have similar homogenized thermal conductivities. For the P shellular family, increasing

Table 6

Temperature contours of architected and graded cellular media along with the minimum and maximum values for Q_r , Q_t and T_{max} . The results of a solid medium are also provided as a baseline for comparison.



the f value from 0 to 0.8 decreased the effective thermal conductivity. Finally, using a case study in 2D, it was shown how the concept of architected functionally graded cellular materials can be used to tune the heat flow and temperature within a cellular medium. While the methodology presented in this paper sheds light on the engineering of thermal conductivity of advanced cellular metamaterials, manufacturable by additive manufacturing technology, this study needs to be further extended to also consider the other properties of cellular materials such as stiffness, electrical conductivity, and permeability in order to evaluate their multi-functional properties. This information will enable designers to develop engineered lightweight multifunctional metamaterials with programmable multiphysical properties in multiple length scales [28,62,63].

Acknowledgements

A.H. Akbarzadeh acknowledges the financial support of McGill University and Natural Sciences and Engineering Research Council of Canada (NSERC) through NSERC Discovery Grant RGPIN-2016-290471. The authors also acknowledge financial support from the Research Center for High Performance Polymer and Composite Systems (CREPEC).

Appendix A. Supplementary data

Supplementary data to this article can be found online at <https://doi.org/10.1016/j.actamat.2019.04.061>.

References

- [1] T.A. Schaedler, W.B. Carter, Architected cellular materials, *Annu. Rev. Mater. Res.* 46 (1) (2016) 187–210.
- [2] A. Akbarzadeh Shafaroudi, S. Rankohi, Multifunctional and multiphysics materials as load-bearing structural components, in: Annual Conference of the Canadian Society for Civil Engineering: Resilient Infrastructure, 2016, pp. 1–9. London.
- [3] L.J. Gibson, M.F. Ashby, *Cellular Solids: Structure and Properties*, Cambridge University Press, 1999.
- [4] A. Öchsner, T. Fiedler, Effective thermal properties of hollow-sphere structures: a finite element approach, in: *Cellular and Porous Materials*, Wiley-VCH Verlag GmbH & Co. KGaA, 2008, pp. 31–71.
- [5] D. Baillis, R.m. Coquard, Radiative and conductive thermal properties of foams, in: *Cellular and Porous Materials: Thermal Properties Simulation and Prediction*, 2008, pp. 343–384.
- [6] I.V. Belova, G.E. Murch, Thermal properties of composite materials and porous media: lattice-based Monte Carlo approaches, in: *Cellular and Porous Materials*, Wiley-VCH Verlag GmbH & Co. KGaA, 2008, pp. 73–95.
- [7] I.V. Belova, et al., Analysis of anisotropic behaviour of thermal conductivity in cellular metals, *Scripta Mater.* 65 (2011) 436–439.
- [8] T. Fiedler, et al., Determination of the thermal conductivity of periodic APM foam models, *Int. J. Heat Mass Transf.* 73 (2014) 826–833.
- [9] J. Gasia, L. Miró, L.F. Cabeza, Materials and system requirements of high temperature thermal energy storage systems: a review. Part 2: thermal conductivity enhancement techniques, *Renew. Sustain. Energy Rev.* 60 (2016) 1584–1601.
- [10] P. Kumar, F. Topin, J. Vicente, Determination of effective thermal conductivity from geometrical properties: application to open cell foams, *Int. J. Therm. Sci.* 81 (2014) 13–28.
- [11] H. Montazerian, et al., Porous scaffold internal architecture design based on minimal surfaces: a compromise between permeability and elastic properties, *Mater. Des.* 126 (2017) 98–114.
- [12] W. Wang, et al., Analytical design of effective thermal conductivity for fluid-saturated prismatic cellular metal honeycombs, *Theoret. Appl. Mech. Lett.* 6 (2016) 69–75.
- [13] P. Ranut, On the effective thermal conductivity of aluminum metal foams: review and improvement of the available empirical and analytical models, *Appl. Therm. Eng.* 101 (2016) 496–524.
- [14] Z. Lu, et al., Elastic properties of two novel auxetic 3D cellular structures, *Int. J. Solids Struct.* 124 (2017) 46–56.
- [15] T.A. Schaedler, et al., Ultralight metallic microlattices, *Science* 334 (6058) (2011) 962–965.
- [16] R. Courant, D. Hilbert, *Methods of Mathematical Physics*, Wiley-VCH Verlag GmbH, 2008 (I–XXII).
- [17] R. Singh, Thermal conduction through porous systems, in: *Cellular and Porous Materials*, Wiley-VCH Verlag GmbH & Co. KGaA, 2008, pp. 199–238.
- [18] T.H. Bauer, A general analytical approach toward the thermal conductivity of porous media, *Int. J. Heat Mass Transf.* 36 (1993) 4181–4191.
- [19] L. Gong, et al., A novel effective medium theory for modelling the thermal conductivity of porous materials, *Int. J. Heat Mass Transf.* 68 (2014) 295–298.
- [20] Z. Hashin, S. Shtrikman, A variational approach to the theory of the effective magnetic permeability of multiphase materials, *J. Appl. Phys.* 33 (10) (1962) 3125–3131.
- [21] T. Fiedler, et al., Optimized Lattice Monte Carlo for thermal analysis of composites, *Comput. Mater. Sci.* 95 (2014) 207–212.
- [22] A.T. Karttunen, J.N. Reddy, J. Romanoff, Micropolar modeling approach for periodic sandwich beams, *Compos. Struct.* 185 (2018) 656–664.
- [23] S.J. Hollister, N. Kikuchi, A comparison of homogenization and standard mechanics analyses for periodic porous composites, *Comput. Mech.* 10 (2) (1992) 73–95.
- [24] N. S. Bakhvalov, G. Panasenko, *Homogenisation: Averaging Processes in Periodic Media*, 1989.
- [25] H.S. Chul, L.J. Woo, K. Kiju, A new type of low density material: shellular, *Adv. Mater.* 27 (37) (2015) 5506–5511.
- [26] D.W. Abueidda, et al., Effective conductivities and elastic moduli of novel foams with triply periodic minimal surfaces, *Mech. Mater.* 95 (2016) 102–115.
- [27] G. Park, et al., Tunable multifunctional thermal metamaterials: manipulation of local heat flux via assembly of unit-cell thermal shifters, *Sci. Rep.* 7 (2017) 41000.
- [28] C. Zhang, et al., Nano-architected metamaterials: carbon nanotube-based nanotubes, *Carbon* 131 (2018) 38–46.
- [29] G. Romano, et al., Temperature-dependent thermal conductivity in silicon nanostructured materials studied by the Boltzmann transport equation, *Phys. Rev. B* 93 (3) (2016), 035408.
- [30] H. Ghasemi, A. Rajabpour, A.H. Akbarzadeh, Tuning thermal conductivity of porous graphene by pore topology engineering: comparison of non-equilibrium molecular dynamics and finite element study, *Int. J. Heat Mass Transf.* 123 (2018) 261–271.
- [31] F.P. Incropera, *Fundamentals of Heat and Mass Transfer*, John Wiley & Sons, 2006.
- [32] M. Matsuura, Gielis' superformula and regular polygons, *J. Geom.* 106 (2) (2015) 383–403.
- [33] A.L. Mackay, Periodic minimal surfaces, *Nature* 314 (1985) 604.
- [34] Y. Deng, M. Mieczkowski, Three-dimensional periodic cubic membrane structure in the mitochondria of amoebaeChaos carolinensis, *Protoplasma* 203 (1) (1998) 16–25.
- [35] Z. Gan, M.D. Turner, M. Gu, Biomimetic gyroid nanostructures exceeding their natural origins, *Sci. Adv.* 2 (2016).
- [36] J. Shin, et al., Finite element analysis of Schwarz P surface pore geometries for tissue-engineered scaffolds, *Math. Probl. Eng.* 2012 (2012), 694194, 13 pages, <http://dx.doi.org/10.1155/2012/694194>.
- [37] S.C. Kapfer, et al., Minimal surface scaffold designs for tissue engineering, *Biomaterials* 32 (29) (2011) 6875–6882.
- [38] J. Lei, Z. Liu, The structural and mechanical properties of graphene aerogels based on Schwarz-surface-like graphene models, *Carbon* 130 (2018) 741–748.
- [39] I. Maskery, et al., Insights into the Mechanical Properties of Several Triply Periodic Minimal Surface Lattice Structures Made by Polymer Additive Manufacturing, *Polymer* 152 (2018) 62–71.
- [40] P.G. Collishaw, J.R.G. Evans, An assessment of expressions for the apparent thermal-conductivity of cellular materials, *J. Mater. Sci.* 29 (9) (1994) 2261–2273.
- [41] T. Fiedler, I.V. Belova, G.E. Murch, Theoretical and Lattice Monte Carlo analyses on thermal conduction in cellular metals, *Comput. Mater. Sci.* 50 (2) (2010) 503–509.
- [42] L. Boldrin, F. Scarpa, R. Rajasekaran, Thermal conductivities of iso-volume centre-symmetric honeycombs, *Compos. Struct.* 113 (1) (2014) 498–506.
- [43] W. Van De Walle, H. Janssen, Validation of a 3D pore scale prediction model for the thermal conductivity of porous building materials, *Energy Procedia* 132 (2017) 225–230.
- [44] G.L. Vignoles, A. Ortona, Numerical study of effective heat conductivities of foams by coupled conduction and radiation, *Int. J. Therm. Sci.* 109 (2016) 270–278.
- [45] V.M. Patel, P. Talukdar, Determination of radiative properties of representative real open cell foam structures using the finite volume method, *Int. J. Therm. Sci.* 132 (2018) 117–128.
- [46] A.H. Akbarzadeh, et al., Electrically conducting sandwich cylinder with a planar lattice core under prescribed eigenstrain and magnetic field, *Compos. Struct.* 153 (2016) 632–644.
- [47] W. Pabst, et al., Young's modulus and thermal conductivity of model materials with convex or concave pores – from analytical predictions to numerical results, *J. Eur. Ceram. Soc.* 38 (7) (2018) 2694–2707.
- [48] J.F. Nye, *Physical Properties of Crystals: Their Representation by Tensors and Matrices*, Clarendon Press, 1985.
- [49] H. Moldenhauer, Integration of direction fields with standard options in finite element programs, *Math. Comput. Appl.* 23 (2) (2018) 24.
- [50] K.P. Vemuri, P.R. Bandaru, Anomalous refraction of heat flux in thermal metamaterials, *Appl. Phys. Lett.* 104 (8) (2014), 083901.
- [51] K.P. Vemuri, P.R. Bandaru, Geometrical considerations in the control and

- manipulation of conductive heat flux in multilayered thermal metamaterials, *Appl. Phys. Lett.* 103 (13) (2013) 133111.
- [52] K.P. Vemuri, F.M. Canbazoglu, P.R. Bandaru, Guiding conductive heat flux through thermal metamaterials, *Appl. Phys. Lett.* 105 (19) (2014) 193904.
- [53] P.R. Bandaru, et al., Layered thermal metamaterials for the directing and harvesting of conductive heat, *AIP Adv.* 5 (5) (2015), 053403.
- [54] D. Zhao, et al., Measurement techniques for thermal conductivity and interfacial thermal conductance of bulk and thin film materials, *J. Electron. Packag.* 138 (4) (2016), 040802–040802-19.
- [55] A. Bouguerra, et al., Measurement of thermal conductivity, thermal diffusivity and heat capacity of highly porous building materials using transient plane source technique, *Int. Commun. Heat Mass Transf.* 28 (8) (2001) 1065–1078.
- [56] L. Gong, et al., Porous Mullite Ceramics with Low Thermal Conductivity Prepared by Foaming and Starch Consolidation, vol. 21, 2014.
- [57] E.T. Afriyie, et al., Textural and thermal conductivity properties of a low density mesoporous silica material, *Energy Build.* 75 (2014) 210–215.
- [58] D.S. Smith, et al., Thermal conductivity of porous materials, *J. Mater. Res.* 28 (17) (2013) 2260–2272.
- [59] H. Niknam, et al., Architected multi-directional functionally graded cellular plates, *Mater. Des.* 148 (2018) 188–202.
- [60] A.H. Akbarzadeh, et al., Dynamic eigenstrain behavior of magnetoelastic functionally graded cellular cylinders, *Compos. Struct.* 116 (2014) 404–413.
- [61] A. Radman, X. Huang, Y.M. Xie, Topology optimization of functionally graded cellular materials, *J. Mater. Sci.* 48 (4) (2013) 1503–1510.
- [62] H. Cui, et al., Three-dimensional printing of piezoelectric materials with designed anisotropy and directional response, *Nat. Mater.* 18 (3) (2019) 234–241.
- [63] J. Shi, A.H. Akbarzadeh, Architected cellular piezoelectric metamaterials: thermo-electro-mechanical properties, *Acta Mater.* 163 (2019) 91–121.